# On the stability of nanovoids in fcc metals and the influence of hydrogen

M. Landeiro dos Reis, Yves Ferro, A. Oudriss, Xavier Feaugas

# On the stability of nanovoids in fcc metals and the influence of hydrogen

M. Landeiro Dos Reis[a], Y. Ferro[b], A. Oudriss[a], X. Feaugas[a]

[a]*La Rochelle UniversitÃľ Laboratoire des Sciences de l'IngÃľnieur pour l'Environnement UMR CNRS 7356 Avenue Michel CrÃľpeau 17000 La Rochelle*
[b]*Laboratoire PIIM Aix-Marseille UniversitÃľ Centre National de la Recherche Scientifique Avenue Escadrille Normandie-Niemen 13397 Marseille France*

**Abstract**

Atomic-scale simulations are used to examine the stability of nanometric vacancy clusters in variety of face centered cubic metals (Au, Ag, Pd, Al, Cu and Ni), according to their shape, their size and the presence of hydrogen. It is shown that whilst in most of metals the stacking fault tetrahedron is the most stable defect in absence of hydrogen, cavities becomes more stable when the concentration of hydrogen is sufficiently large to cover the internal surfaces. The (100) surfaces are found to be the less energetic, which favors vacancy clusters with cuboid shape in the metals concerned here. The simulations are shown to agree well with theoretical predictions provided that the theory is parametrized with surface and bulk energies conformed to the atomistic models. The affinity between hydrogen and cuboid cavities has also been confirmed by the computation of hydrogen solubility, which is neatly enhanced in the vicinity of these cavities. Our study paves the way toward the comprehensive atomistic-based predictions for micro-structure in hydrogen-rich metals.

*Keywords:* Nanovoid, defect surface energy, hydrogen solubility

## 1. Introduction

Nanovoids are commonly observed in a wide variety of metals. The formation of these defects is primarily ascribed to vacancy aggregation a

*Email address:* mlandeir@univ-lr.fr (M. Landeiro Dos Reis)

process often triggered by specific heat treatments or fluid environments [18, 11, 38, 39, 66, 108, 81, 40, 107, 84, 96], irradiation [18, 10, 38, 39, 79], and even deformation [18, 48, 104, 38, 39, 60, 13]. Vacancy clustering may also result from dislocation interactions [18, 48, 104, 38, 39, 60, 13]. The nanovoids are known to play a significant role in various material processes, including corrosion, irradiation swelling, heterogeneous phase precipitation, creep and fatigue deformation and hydrogen embrittlement [21, 65, 106, 90, 7, 57, 44, 45, 73, 41, 99, 61, 19, 8, 17, 71, 30]. They notably modify the mechanical properties, affecting both elastic and plastic properties [77, 69, 29, 3, 45].

The concentration, size, and shape of nanovoids are highly sensitive to various factors such as temperature, mechanical strain, impurities, chemical composition and environment (gas, aqueous...) [18, 11]. Among these factors, the presence of gas seems to be the preponderant factor [18, 11]. Experimental studies have shown that a gaseous environment stabilizes vacancies and voids [18, 11, 26, 27, 9]. Conversely, simulation studies have demonstrated that hydrogen interstitials are trapped by vacancies due to the attractive interaction between these point defects, thereby promoting the formation of super-abundant vacancies or small vacancy-hydrogen complexes [64, 56, 23, 62, 55, 54, 89, 49, 24, 110, 26]. Although significant efforts have been made to understand the clustering of vacancies [93, 1, 70, 103, 34, 68], only a few studies have taken into account the effect of hydrogen [20, 89, 56, 22, 95] and globally focus on the first steps of clustering, *i.e* few vacancy defects and not nanometer scale defects.

In the present study, we employ atomic-scale simulations with empirical potentials to examine the stability of vacancy clusters in various fcc metals (Au, Ag, Pd, Al, Cu, Ni). We have compared the formation energies of the most common shapes of cluster according to their size. The stacking-fault tetrahedra (SFT) and octahedron clusters are more favorable, except in the case of Al, where the large stacking fault energy leads to a unstable SFT. We analyzed our simulation results by exploring the defect surface energies. This enables us to establish a satisfactory comparison between the stable shapes in simulations and the predictions made from Wulff theory [4]. We subsequently investigated the impact of gaseous hydrogen, scrutinizing its influence on the stability of vacancy clusters in Ni and Al systems. In presence of hydrogen, clusters tend to adopt a cubic-shaped configuration, a preference that has been elucidated by examining defect surface energies.

Additionally, employing standard approximation for ideal gas, we have estimated the solubility of hydrogen in the vicinity of vacancy clusters, taking

into account the shape of voids, their sizes and the temperature. Our results reveal that hydrogen solubility predominantly correlates with cluster size, although it also exhibits a sensitivity to cluster shape. Consistent with our numerical simulations, our theoretical analysis indicates that the hydrogen solubility is maximum around cubic-shaped clusters in Ni and rises with increasing temperature.

## 2. Method

### *2.1. Empirical potentials*

Table 1: Properties of the studied fcc metals computed here with molecular static (MS). $a_0$ is the lattice parameter, $E_f$ is the vacancy formation energy, $\Gamma$ is the maximum staking fault energy, and $\gamma_{100}$, $\gamma_{110}$ and $\gamma_{111}$ are the surface energies of {100}, {110} and {111} surfaces. The comparison of these values with existing literature, whether derived from experiments or Density Functional Theory (DFT), is detailed in the corresponding reference for each potential.

| | Au [75] | Ag [102] | Pd [28] | Al [47] | Al [2] | Cu [58] | Ni [2] |
|---|---|---|---|---|---|---|---|
| $a_0$ (Å) | 4.08 | 4.09 | 3.88 | 4.03 | 4.05 | 3.62 | 3.52 |
| $E_f$ (eV) | 0.88 | 1.10 | 1.25 | 0.68 | 0.52 | 1.27 | 1.59 |
| $\Gamma$ ($\frac{\text{meV}}{\text{Å}^2}$) | 28 | 18 | 17 | 130 | 99 | 44 | 89 |
| $\gamma_{100}$ ($\frac{\text{meV}}{\text{Å}^2}$) | 83 | 59 | 129 | 63 | 63 | 84 | 129 |
| $\gamma_{110}$ ($\frac{\text{meV}}{\text{Å}^2}$) | 89 | 63 | 141 | 69 | 72 | 92 | 147 |
| $\gamma_{111}$ ($\frac{\text{meV}}{\text{Å}^2}$) | 80 | 54 | 125 | 57 | 62 | 77 | 120 |

Table 2: Elastic properties of the investigated fcc metals computed with empirical potentials, including the elastic constants $C_{11}$, $C_{12}$, and $C_{44}$, the anisotropy ratio $A$, anisotropy factor $H$, shear modulus $\mu$, bulk modulus $B$, Poisson ratio $\nu$, Burgers vector $b$.

| | Au [75] | Ag [102] | Pd [28] | Al [47] | Al [2] | Cu [58] | Ni [2] |
|---|---|---|---|---|---|---|---|
| $C_{11}$ (GPa) | 205 | 124 | 247 | 119 | 114 | 170 | 247 |
| $C_{12}$ (GPa) | 168 | 94 | 200 | 63 | 62 | 123 | 147 |
| $C_{44}$ (GPa) | 49 | 46 | 56 | 33 | 32 | 76 | 125 |
| $\mu$ (GPa) | 37 | 34 | 43 | 31 | 29 | 55 | 95 |
| $\nu$ | 0.40 | 0.35 | 0.41 | 0.33 | 0.34 | 0.32 | 0.28 |
| $\mu b/\Gamma$ | 24 | 34 | 43 | 4 | 5 | 20 | 17 |

The force fields, derived from the Embedded Atom Method (EAM), are computed using the Large-scale Atomic/Molecular Massively Parallel Simulator (LAMMPS) [72]. The potential of Pun is employed for Au [75], that of Williams *et al.* for Ag [102], Hale *et al.* for Pd [28], Liu *et al.* and Angelo *et al.* for Al [47], Mishin *et al.* for Cu [58], and Angelo *et al.* for Ni [2]. The interaction between hydrogen and the metals (Ni and Al) is accounted for using the Angelo *et al.* potential [2]. The atomic positions are relaxed using the Fast Inertial Relaxation Engine (FIRE) algorithm [6] until a force criterion of 0.1 meV/Å is met. The fundamental properties of the metal, as provided by the potentials, are listed in Table 1.

The elastic properties of the metals have been determined using the Voigt Average, where $\nu$ is the Poisson ratio and $\mu$ stands for the shear modulus. These properties are calculated using the following equations :

$$\begin{cases} \nu = (C_{11} + 4C_{12} - 2C_{44})/2(2C_{11} + 3C_{12} + C_{44}) \\ \mu = (C_{11} - C_{12} + 3C_{44})/5 \end{cases} \quad (1)$$

*2.2. Simulation cell*

We build perfect cubic simulation cells containing at most $N_{at} \simeq 4.10^6$ atoms in the standard orientation $x = [100]$, $y = [010]$ and $z = [001]$. The typical size in each direction is 50 nm which allows us to avoid finite size effect due to elastic interactions. Subsequently, we introduced a vacancy defect and relaxed the atomic forces until the force criterion was reached. Fig. 1 shows the four nanovoid shapes tested (spherical, octahedron truncated or not, tetrahedron, cubic), that contains typical shapes observed in fcc crystals [66, 39, 10, 96]. These vacancy clusters are introduced in the simulation cells by removing atoms within the defined geometric region that characterizes the defect. It is worth noticing, that truncated octahedron correspond to the predicted Wulff shape, as discussed later (Sec. 4.2). We tested two different types of truncation: severely truncated octahedron (ST), with 40% truncation, and moderately truncated octahedron (MT), with 20% truncation (Fig. 1(d)).

To complete our set of defect, we constructed stacking fault tetrahedras (SFT) commonly found in most fcc crystals [18, 39, 84]. We employed the method presented in Ref. [37] and used the dislocation analysis (DXA) tools from OVITO to visualize and analyze the atomic configurations [88]. Unlike tetrahedral shaped nanovoids, stacking fault tetrahedra (SFT) are not empty and are composed of stacking faults bounded by dislocations.

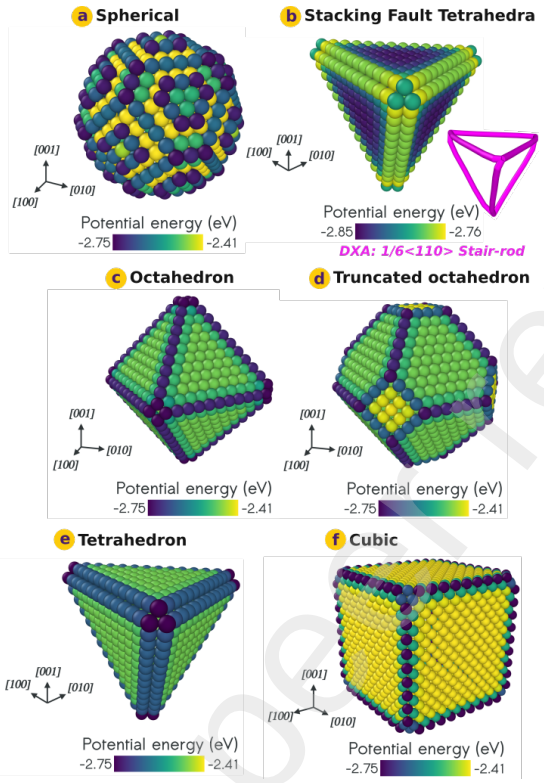


Figure 1: Geometry studied: (a) spherical, (b) SFT, (c) octahedron (d) truncated octahedron, (e) tetrahedron and (f) cubic. Only defected atomic positions are shown. The color coding correspond to the potential energy per atom obtain after relaxation in Ag crystal.

In principle SFT are composed of six stair-rod dislocations. However, beyond a critical size, the SFTs introduced in our simulation cells become truncated and form Shockley partials along the energy minimisation as already discussed in literature [35]. In Fig. 2(a) we have reported two examples of the different types of SFTs in Pd: the complete SFT made of stair-rods below the critical size and the truncated SFT composed of stair-rods associated with Shockley partials. The critical size of this transition between complete and truncated SFT depends on the elastic properties of the metal, detailed in Table 2, and it can be estimated from the theory developped by Jossang and Hirth [35]. In the case of Pd, we obtained complete SFTs between 10 to 136 vacancies. In Ni, complete SFTs could be formed from 10 to 2926 vacancies, whilst for Cu, we obtained complete SFTs from 28 to 3655 vacancies. In contrast, for both Au and Ag, complete SFTs consistently formed

starting from 28 vacancies and we did not found any transformation for all sizes beyond. In the specific case of Al, complete SFTs were observed at 10, 190, 253, 406, and 496 vacancies (Fig. 2(b)). For other vacancy numbers in Al, SFTs are highly truncated, as shown in Fig. 2(b) for cases with 28, 55, and 136 vacancies. However, when the vacancy count reaches a certain threshold of 595, we observe exclusively the formation of Franck dislocation loops, as illustrated in Fig. 2(b).

To investigate the impact of hydrogen on the cluster, we introduced hydrogen atoms in our simulations as follows. We essentially worked in the case where each vacancy is replaced with a single hydrogen atom. After relaxation, the nanovoid displays a surface adorned with hydrogen interstitial atoms and contains $H_2$ molecules. In pure metals DFT studies have shown that high concentrations of hydrogen enhance its trapping by vacancies [89]. That promotes the formation of superabundant vacancies wherein all six octahedral sites first neighboring the vacancy are occupied by hydrogen. So in order to determine the role of hydrogen pressure we have also tested the case, where each vacancy is replaced by six hydrogen. In practice we placed the supplementary hydrogen atoms at the first octahedral sites neighboring the metal atoms that have been removed. The results indicate that once the surface is saturated, there is no significant change of nanovoid stability against concentration of hydrogen, or equivalently hydrogen pressure (See Appendix Appendix A).

## 3. Simulation results

### *3.1. Formation energy*

The formation energy of the n-vacancy defect is :

$$e_f^n = E_d - n_{fcc}e_0 - n_H\frac{e_{H_2}}{2}. \tag{2}$$

where $E_d$ is the energy of the defected cell, $e_0$ is the energy per atom of the perfect simulation cell, $n_{fcc}$ is the number of fcc atoms in the defected cell, $n_H$ is the number of hydrogen atoms and $e_{H_2}$ is the potential energy of the $H_2$ molecule.

We reported the results for Ni in Fig. 3(a) and for Au (Fig. 3(b). Those obtained for the other fcc metals show very similar trends. The formation energy increases with the defect size (Fig. 3), and the rate of this increase varies with the nanovoid shape. One important observation is that the most

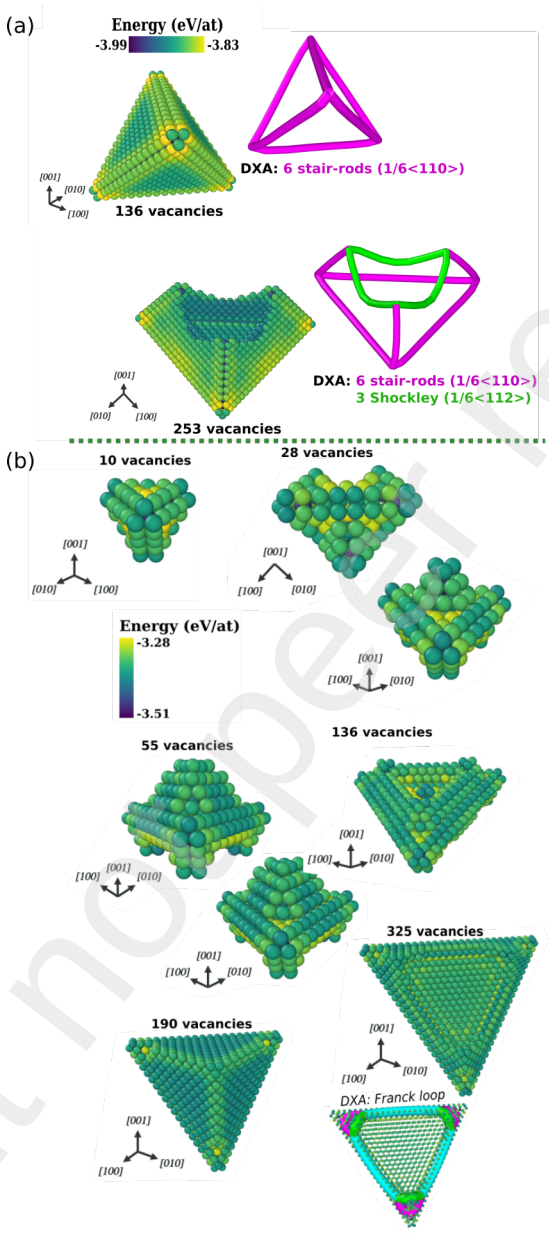


Figure 2: (a) SFT defects in Pd computed with Hale *et al.* potential for several size (vacancy number). (b) SFT and unfaulting Franck loop in Al computed with Angelo *et al.* potential for several sizes (vacancy number).

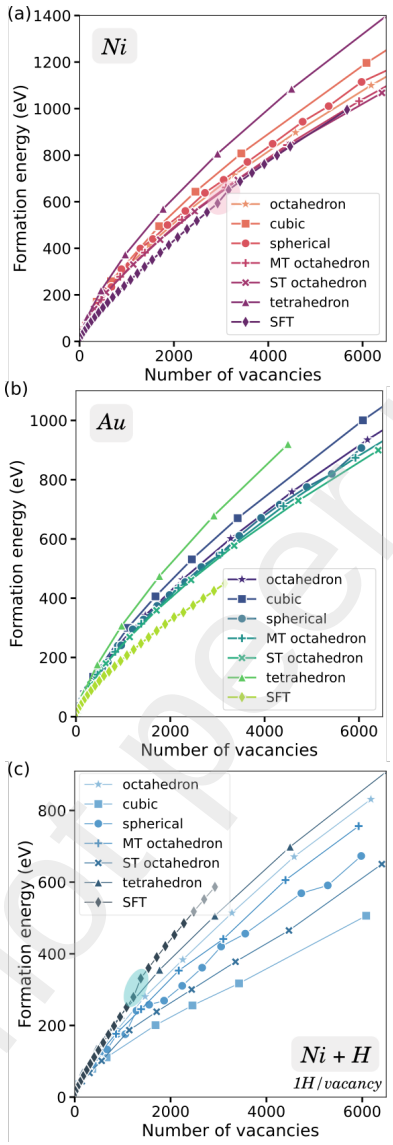


Figure 3: Formation energy for various vacancy cluster shapes, *i.e* octahedron, cubic, spherical, moderately truncated (MT) octahedron, severely truncated (ST) octahedron, tetrahedron and stacking fault tetrahedra (SFT), and the size (number of vacancies) in (a) Ni and (b) Au (c) Ni- H systems. Results for another hydrogen concentration is shown Fig. A.14 and the results for Cu and Ag are similar to those observed for Ni and the results observed for Pd and Al are similar to those of Au (See Appendix Appendix A: Fig. A.12 and Fig. A.13).

favorable defect for all systems is the one containing dislocations, i.e., SFT (stair-rods or Shockley partials depending on the defect size) and Franck loops (for Al). This may be ascribed to the larger degree of freedom for local atomic relaxation near dislocation cores compared to the more constrained environment near the surfaces of nanovoids. A change in slope is observed in the evolution of the formation energy with respect to the number of vacancies in the case of SFT (as indicated by the pink region in Fig. 3(a)). This change occurs at the critical size, beyond which SFT decomposes into stair-rod dislocations and Shockley partials (see Fig. 2(a)). We have noticed that in the Au, Pd, and Al systems (Fig. 3(b)), there is a significant disparity in energy terms between SFT/Franck loops and other vacancy cluster defects, compared to the Ni, Cu, and Ag systems (Fig. 3(a)). In both the Ni and Cu systems, truncated octahedra emerge as the preferred defects after a substantial number of vacancies (around 2500 for Cu and 5000 for Ni), as shown in Fig. 3 (a) and Fig. A.13. Among the other studied metals (Ag, Au, Pd, Al), truncated octahedra remain the second most favorable defect (Fig. 3 (a), Fig. A.12, Fig. A.13). Additionally, Fig. 3 shows that moderately truncated (MT) octahedra and severely truncated (ST) octahedra yield similar results. Therefore, it appears that in this case the formation energy of truncated octahedra is not significantly influenced by the degree of truncation.

To complete our study, we have additionally computed the interaction energy. This was achieved by employing the following equation:

$$E_{int} = E_{d+1V} - E_d - E_0 - E_{1V} \tag{3}$$

where $E_{d+1V}$ represents the energy of the cell with both a nanovoid and a vacancy, $E_d$ denotes the energy of the cell with only the nanovoid, $E_0$ corresponds to the energy of the perfect crystal, and $E_{1V}$ stands for the energy of the cell with a single isolated vacancy. This interaction energy was determined for different possible positions of the vacancy relative to the nanovoid. The results are shown in Fig. 4, where the color of an atom at coordinates (x, y, z) represents the actual interaction energy between a vacancy situated at the very same position and the nanovoid. The calculation was repeated for each position. It is worth noticing that the interaction energy shows a subtle anisotropy, being smaller in (100) directions than in (110) ones. Fig. 4 confirms that there exists an attractive interaction between nanovoids and vacancies as it was also reported in previous studies [33, 67, 100, 45].

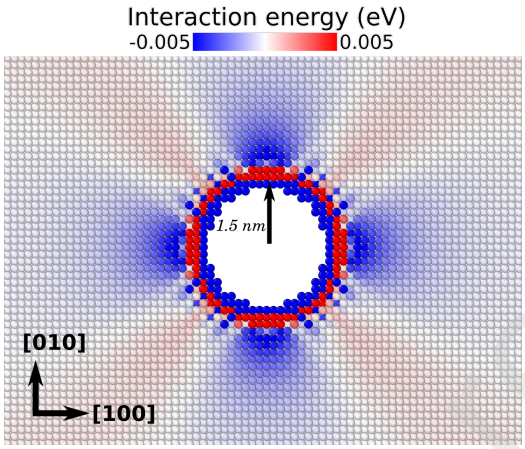


Figure 4: Interaction energy map between a vacancy and a spherical cluster of 1289 vacancies (radius, r = 1.5 nm) in Ni.

The impact of hydrogen on the formation energy of defects is now quantified in a matrix of Ni. The results have been reported in Fig. 3(c). The formation energy of the H-nanovoids is notably smaller than that for "pure" vacancy clusters shown in Fig. 3(a). It demonstrates the stabilization of vacancy clusters in presence of hydrogen. Such a result can be related to the attractive interaction between hydrogen and vacancies in Ni [56]. In contrast, the effect of hydrogen on SFT is less pronounced, even though the critical size for the transition from complete SFT (only stair-rods) to truncated SFT (with Shockley partials) is lower in the presence of hydrogen. The transition has been pointed out in Fig. 3(c) by a shaded blue area whilst in Fig. 3 it was situated in the shaded pink area. As it was observed with no hydrogen, SFT's are the most stable defects for small sizes (up to 91 vacancies and so 91 H atoms, which corresponds to a lenght of 3 nm). However for larger clusters the SFT's become less stable than nanovoids that are favored by the presence of hydrogen. For clusters with vacancy number between 100 to 565, severely truncated octahedra are the most stable. They correspond to a cluster size with a height between 1.8 nm and 2.5 nm. Interestingly, in contrast to pure vacancy clusters, the results for severely truncated octahedra differ from those obtained for moderately truncated octahedra in presence of hydrogen. Since the main difference between severely and moderately truncated octahedra with same number of vacancy comes from the area of planar surface {111} and {100}, we can thus incriminate the importance of hydrogen on the

surface energies, especially on the ratio $\gamma_{111}/\gamma_{100}$. Beyond 565 vacancies the cubic shape is the most stable. Hence, we can again question the importance of hydrogen on {100} surfaces. We have tested another hydrogen concentration, corresponding to 6 Hydrogen per vacancy (see Appendix Appendix A, Fig. A.14). We noticed that once the surface is saturated, there is no significant change of nanovoid stability against concentration of hydrogen.

## 4. Discussion

### *4.1. Formation energy of stacking fault tetrahedra (SFT)*

Stacking fault tetrahedra (SFT) were the matter of numerous studies in the literature [48, 38, 93, 1, 70, 69, 97, 98, 103, 34, 37, 35, 12]. According to our careful reading no study has hitherto reported a systematic investigation over a broad range of elastic constants and stacking fault energy. We performed such a work in order to test the relevance of the analytical model proposed by Jossang and Hirth [35] to express the SFT formation energy. According to this theory the SFT formation energy can be expressed as follows :

$$\frac{E_f^{SFT}}{\mu b^3} = P(\nu, b, L)\left[2\ln\left(\frac{\alpha L}{b}\right) + M(\nu)\right] + \sqrt{3}\left(\frac{\Gamma}{\mu b}\right)\left(\frac{L}{b}\right)^2 \tag{4}$$

where one recognizes the shear modulus $\mu$, the Burgers vector $b$, the stacking fault energy $\Gamma$, the poisson ratio $\nu$, and the SFT size denoted by $L$. The dimensionless quantities $P(\nu, b, L)$ and $M(\nu)$ are given by :

$$P(\nu, b, L) = \frac{1}{12\pi(1-\nu)}\left(\frac{L}{b}\right) \text{ and} \tag{5}$$

$$M(\nu) = \frac{2}{3} + 2\ln(2) + 2\sqrt{2}\nu\left(2\arctan(\sqrt{2}) - \arctan(2\sqrt{2})\right). \tag{6}$$

Table 3: Adjusted parameter $\alpha$ in the Jossang and Hirth model (Eq. 4).

| | Au | Ag | Pd | Cu | Ni |
|---|---|---|---|---|---|
| $\alpha$ | 5 | 8 | $10^4$ | 6 | 0.5 |

The parameters $\Gamma$, $\mu$ and $\nu$ have been reported in Tab. 2. The generalized stacking fault (GSF) energy curve from which $\Gamma$ is deduced is plotted in Fig. 5(a). Aside from $\alpha$ that is an adjustable parameter in the theory, all

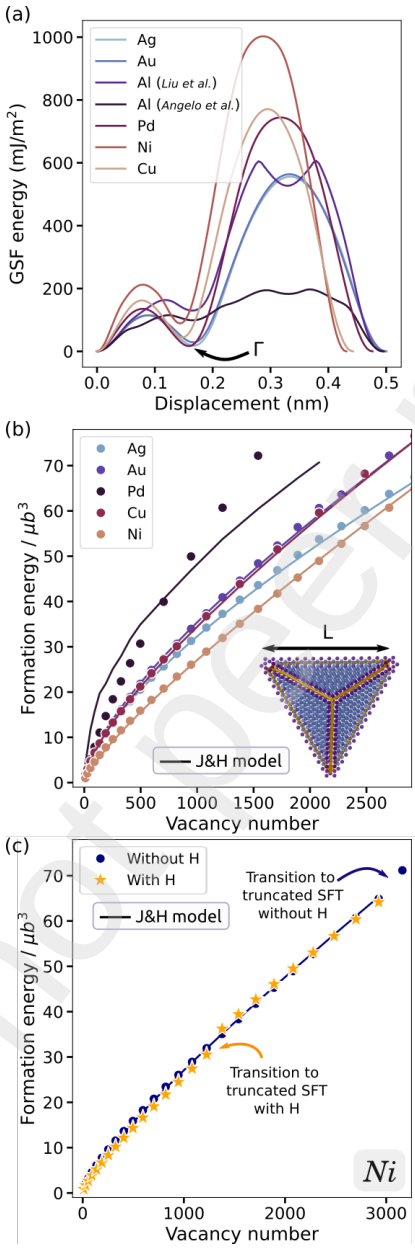


Figure 5: (a) Computation results of the generalized stacking fault energy (GSF) for all the fcc metal studied. Comparison between the formation energy of SFT deduced from our simulation to Jossang and Hirth model (Eq. 4) (b) for each fcc metals (c) for Ni and Ni-H systems.

the other parameters were computed from dedicated simulations (see Table. 3), independent from our computations for cavities. Excepted for Pd, the predictions established from Jossang and Hirth model (Eq. 4) aligns well with our simulation data. The extremely high value of the parameter $\alpha$ associated to Pd in comparison to other metals can be attributed to the lack of precision of the interatomic model employed here. Actually this model predicts a ratio $\Gamma/\mu b$ (Table 2) significantly higher than experimental data [80]. The inability of Jossang and Hirth model to reproduce simulations would indicate that the theory applies in a limited range of parameter where $\Gamma/\mu b$ is not too high.

Fig. 5 shows the Jossang and Hirth model's ability to reproduce the formation energy evolution against SFT size (expressed in vacancy number). For larger SFT, the non-linear part distinctly depends on the stacking fault ribbon size $\mu b/\Gamma$.

The comparison between the formation energy of SFT with and without hydrogen realized in Fig. 5(c) shows that the impact of hydrogen is negligible at the concentration tested here. We remarked yet that the transition towards truncated SFT happens at a smaller size in the presence of hydrogen. Results for higher hydrogen concentration have been presented in Appendix Appendix A, Fig. A.14. We noticed that for larger concentration the formation energy of SFT increases which disfavors SFT in regard of other cavities.

### *4.2. Surface energy*

To demonstrate that the stable shape of the vacancy clusters under hydrogen exposure is directly related to the fact that hydrogen modify the surface energy of metals we analysed the surface energy of our defects. Using the framework established for nanoparticles [59], and applying the concept to nanovoids, we can define the surface energy of defects, denoted by $\Gamma_d$, as follows:

$$\Gamma_d = \frac{e_f^n}{S_d}, \tag{7}$$

where $S_d$ denotes the surface area of the defects, determined from the atomic configurations of the relaxed defect cells using the alpha-shape algorithm implemented in OVITO [87]. $S_d$ depends on both size and shape of the defects, as shown in Fig. 6. The surface area for stacking fault tetrahedra (SFT) is much larger than that for vacancy clusters with an equivalent number of vacancies, as illustrated Fig. 6. A sharp step appears clearly along the curve

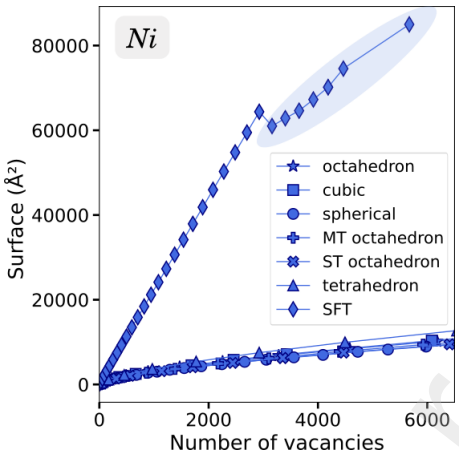


Figure 6: Surface of Ni defects according to their size and shape, *i.e* octahedron, cubic, spherical, moderately truncated (MT) octahedron, severely truncated (ST) octahedron, tetrahedron and stacking fault tetrahedra (SFT).

for $S_d$ at the transition from complete to truncated SFT's, highlighted by a shaded blue area in Fig. 6.

Fig. 7 shows the surface energy of defects in Ni. Results are very similar in other fcc metals (see Appendix Appendix B, Figs. B.15, B.16, B.17). As formation energies (Fig. 3), the surface energies are sensitive to cluster shape. If we consider only the case of pure vacancy clusters, SFT being drastically different (Fig. 7), our results for surface energies correlate with those found for formation energies Fig. 3. In pure Ni the octahedral-shaped clusters correspond to the lowest surface energy, which indicates their more favorable configuration (Fig. 7 (a)). The surface energy associated with each defect shape appears to converge towards an asymptotic value beyond a certain size. These values can then be compared to the surface energies of the primary crystallographic planes, $\gamma_{100}$, $\gamma_{110}$ and $\gamma_{111}$, that have been computed independently in dedicated simulations and reported in Table 1. In pure Ni, it can be noticed that the surface energies of the clusters are generally lower than the $\gamma_{100}$, $\gamma_{110}$, and $\gamma_{111}$ values (Fig. 7 (a)). We interpret such a difference by the fact that at cluster surfaces the atoms have more degrees of freedom to relax into more stable configurations, possibly through surface reconstruction as observed for nanoparticles [78], although we admit that further investigations would be required to conclude.

The SFT surface energies are considerably lower than those for vacancy

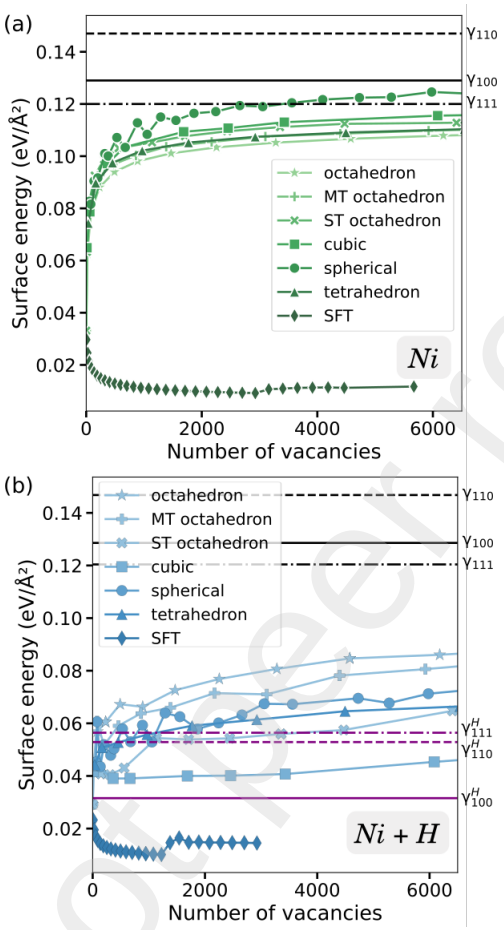


Figure 7: Surface energy of Ni defects according to their shapes, *i.e* octahedron, moderately truncated (MT) octahedron, severely truncated (ST) octahedron, cubic, spherical, tetrahedron and stacking fault tetrahedra (SFT) (a) without or (b) with H (symbols). Surface energies of Ni (see Tab. 1, Fig. 8(b),and Appendix Appendix B: Fig. B.19 and Fig. B.20) are plotted for comparison (lines).

clusters because of their relatively high surface-to-vacancy ratio (Fig. 6). The presence of dislocations also enables more possibilities for energy relaxation.

We compared our simulations with the predictions from Wulff theory [32, 50, 105] based on the surface energies of the primary crystallographic planes given in Table 1. To achieve this, we used a Python package for Wulff constructions [76] and we calculated the Wulff shape for each fcc metal. Our results were reported in Fig. 8(a). Wulff theory predicts a truncated

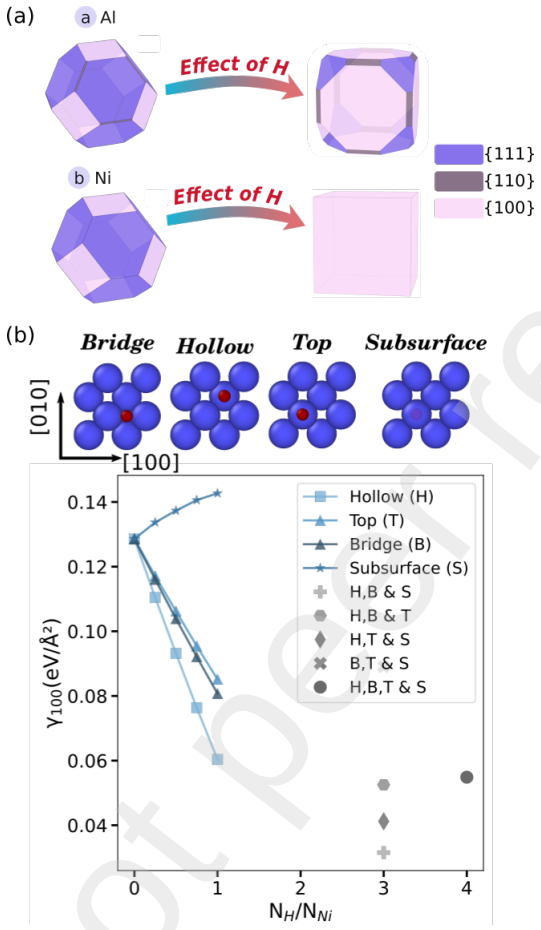


Figure 8: (a) Wulff construction [76] for Al and Ni with and without hydrogen. The shapes for the other metals can be found in Appendix Fig. B.18. (b) Surface energy for {100} plane surface computed for Ni according to the site occupied by the hydrogen atom on the surface (Hollow (H), Top (T), Bridge (B), subsurface (S)) or a combination of these sites (H, B & S occupied or H, B & T etc) and the ratio of the number of hydrogen atoms, quoted $N_H$, to the number of surface Ni atoms, $N_{Ni}$. The atomic configurations for each site are illustrated for the case $N_H = 1$ (atom colored in red) and $N_{Ni} = 4$ (atoms colored in blue). Other orientations can be found in Appendix Appendix B.

octahedral shape for all fcc metals studied here, with different proportion for the {110} plane. The predictions of the theory correspond to atomistic simulations. The agreement is particularly good for large sizes (Fig. 3 and Appendix Appendix A).

Since the surface energy strongly depends on the presence of hydrogen

[5, 25, 43, 92] we computed the primary surface energies $\gamma_{100}$, $\gamma_{110}$, and $\gamma_{111}$ for different hydrogen absorption sites, conventionally referred to as Bridge (B), Hollow (H), Top (T) and subsurface. This glossary is inherited from the literature [5, 25, 43, 92] and we illustrated each configuration in Fig. 8(b). Additionally, we considered the impact of the ratio between the number of adsorbed hydrogen atoms, denoted as $N_H$, to the number of surface Ni atoms, denoted as $N_{Ni}$ (see Fig. 8(b) and Appendix Appendix B). To achieve this, we have constructed simulation cells with free surfaces, forming a slab containing symmetrically distributed hydrogen atoms on each free surfaces. We have tested configurations ranging from ($N_H/N_{Ni} = 0.25$) to ($N_H/N_{Ni} = 1$) with hydrogen atoms situated in specific sites (B, H, T, or S). Additionally, we explored scenarios where hydrogen atoms occupy all $I, J, K$ sites (I, J, K = B, H, T, or S, with I $\neq$ J $\neq$ K) simultaneously, resulting in a ratio $N_H/N_{Ni} = 3$. We also investigated cases where hydrogen atoms simultaneously occupied all sites B, H, T, and S, thence leading to $N_H/N_{Ni} = 4$. We expressed the surface energy as follows :

$$\gamma_{hkl} = \frac{E_s - n_{fcc}e_0 - n_H e_{H_2}/2}{2S_{hkl}}, \tag{8}$$

with $E_s$ as the energy of the simulation cell containing free surfaces of $\{hkl\}$ orientation and $S_{hkl}$ as the surface area. Our results have been reported in Fig. 8(b). Clearly the more favorable situation corresponds to an hydrogen situated in hollow configuration (denoted by (H) in Fig. 8(b)), in agreement with more precise calculations based on density functional theory, as detailed in the work realised by Traisnel et al. [92]. In presence of of hydrogen the surface energy of the primary crystallographic planes decreases as it was already observed for vacancy clusters in Fig. 6(b). Our results agree well with previous studies and confirm that hydrogen stabilizes vacancies [101, 94, 74, 11, 18, 26, 27, 9].

We used Wulff theory with the lowest surface energy $\gamma^H_{100}$, $\gamma^H_{110}$ and $\gamma^H_{111}$ to determine the more stable shape of vacancy cluster. The theory predicts clearly a cubic shape for both Al and Ni as reported in Fig. 8(a). It confirms the results reported Fig. 7(b), where it was shown that cuboid are the more stable shape of vacancy cluster when hydrogen is present at the surfaces whilst the SFT is more stable in pure metals as found in Fig. 3(c).

*4.3. Impact of hydrogen on the vacancy cluster elastic field*

We found that the presence of H changes significantly the elastic relaxation of the crystal around defects.

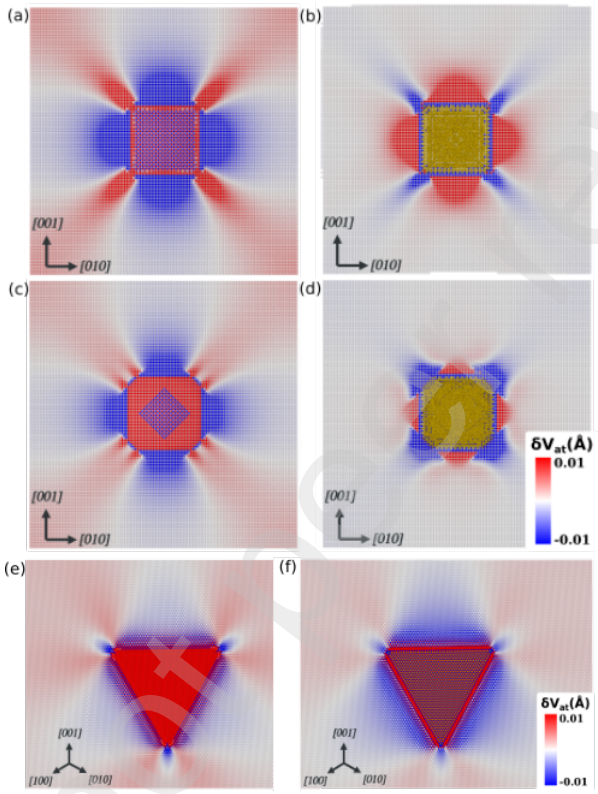


Figure 9: Variation of the atomic volume in the vicinity of cuboid vacancy cluster (a) without H and (b) with H, in Ni. Results for truncated octahedra are shown in (c) without H and in (d) with H and in vicinity of SFT (e) without H and (f) with H.

To visualize this effect, we quantified the alteration of the crystal through the atomic volume in comparison to perfect crystals using the Voronoi formalism [46]. We denoted the volume variation by:

$$\delta V_{at} = V_{at} - V_0, \tag{9}$$

with $V_{at}$ the atomic volume that depends on the lattice distortion and $V_0$ the value of the atomic volume in the perfect relaxed structure. This formulation allowed us to represent the local lattice distortion in the vicinity of defects.

Fig. 9 presents the spatial distribution of $\delta V_{at}$ surrounding the vacancy clusters. The panels (a) and (b) show cuboid clusters while panels (c) and (d) show truncated octahedra. In Ni vacancy clusters devoid of hydrogen, $\delta V_{at}$ takes negative value along the {100} directions, as indicated by the blue coloration in Fig. 9. This indicates a compressive strain in the Ni lattice along these directions, thereby promoting the absorption of vacancies. In the {110} directions, $\delta V_{at}$ displays positive values in the vicinity of nanovoids, as indicated by the red coloration on Fig. 9. This signifies a state of tensile strain in the Ni lattice within this region, rendering vacancy absorption less favorable.

When hydrogen is present in nanovoids, we observed a reversal in the areas of tensile and compressive strain. This suggests a modification in the local anisotropy of defect absorption. Thence vacancy absorption would now be favored in the {110} directions. Another noteworthy observation is the screening of elastic distortion in the presence of hydrogen as the colored areas extend over shorter distances in Figs. 9 (b) and (d) than in Figs. 9(a) and (c). It may result in a reduction of the long-range interaction between nanovoids and other defects. Hence, the presence of hydrogen may influence the interaction between dislocations and vacancy clusters, by screening the long range interactions, and thus influence the mechanical properties. On the basis of the present results we believe that the balance between softening and hardening of fcc metals could be achieved according to the concentration of hydrogen in nanovoids. Computations to study the dislocation depinning from such defects [3, 16] or nanoindentation [15] would be necessary to verify our belief. The screening effect stems from the counterbalance between atomic network contraction near vacancies and the dilation induced by hydrogen atoms. Fig. 9(e-f) presents the same color mapping as in Fig. 9 but for SFT. Unlike nanovoids, the introduction of hydrogen does not seem to exert a discernible effect on the long-range elastic distortion not on the anisotropy of the elastic field. The elastic distortion remains predominantly associated to to the presence of dislocations.

### *4.4. Hydrogen solubility*

To determine hydrogen solubility in metals where vacancy clusters are present, we imposed equality between the chemical potential of gaseous hydrogen present inside nanovoids, denoted by $\mu_g$, and the chemical potential of hydrogen situated in interstitial sites in the crystal lattice, denoted by $\mu_{sol}$.

The solubility $X_{int}$ is defined as follows[31, 92]:

$$X_{int} = \gamma \exp\left[-\beta(G_{sol} - \mu_g/2)\right], \tag{10}$$

where $G_{sol}$ is the free energy of hydrogen situated inside the crystal, $\beta = 1/(k_B T)$ and $\gamma = 1$ corresponds to the number of hydrogen in octahedral site per metal atom in the fcc lattice. With the approximation that gaseous hydrogen is an ideal gas, we can write:

$$\mu_g = \mu_g^0 + k_B T \ln \frac{P}{P_0} \tag{11}$$

where $\mu_g^0$ represents the standard chemical potential of hydrogen, $P_0$ denotes the standard pressure, conventionally set at 1 bar and $P$ is the hydrogen pressure supposed to be equal to the surface pressure at thermodynamical equilibrium (Appendix Appendix C).

The total Gibbs free energy encompasses contributions from vibrational ($G_g^{vib}$), rotational ($G_g^{rot}$), and translational ($G_g^{rot}$) motion modes, thus, we have:

$$\mu_g^0 = G_g = G_g^{vib} + G_g^{rot} + G_g^{trans,0}. \tag{12}$$

According to the harmonic approximation $G_g^{vib}$ can be written as:

$$G_g^{vib} = \frac{h\nu_{H_2}}{2} + k_B T \ln(1 - \exp(-\beta h \nu_{H_2})) \tag{13}$$

where $\nu_{H_2}$ is the vibrational frequency of $H_2$ molecule. If one assumes that hydrogen molecule can rotate freely, i.e. with no interaction, we have :

$$G_g^{rot} = k_B T \left[1 - \ln\left(\frac{8\pi^2 I}{h^2 \sigma \beta}\right)\right] \tag{14}$$

where $I = m_{H_2} d_{H_2}^2/2$ represents the moment of inertia, and $\sigma = 2$ is a parameter accounting for the rotational symmetry of $H_2$ molecule. In our simulations, the mass of hydrogen molecule $m_{H_2} = 2.67 \times 10^{-27}$kg and the equilibrium distance between hydrogen $d_{H_2} = 0.74$. The vibrational frequency have been computed using the code phonopy [91] which gives $\nu_{H_2} = 13.18 \times 10^{13}$Hz, in agreement with computations based on DFT [109, 53] (Appendix Appendix D). We neglected anharmonic quantum effects, acknowledging that

a more thorough examination would be required [14]. The translational free energy is given by ideal gas theory :

$$G_g^{trans} = k_B T \left[ \frac{3}{2} - \ln \left( \left( \frac{2\pi m_{H_2}}{\beta h^2} \right)^{3/2} V \right) \right] \tag{15}$$

where $V = 1/(\beta P)$ and $V = 1/(\beta P_0)$ for $G_g^{trans,0}$. The free energy of hydrogen situated inside the crystal with these approximation is :

$$G_{sol} = E_H^{sol} + \sum_{\nu} \left[ \frac{h\nu}{2} + k_B T \ln \left( 1 - \exp(-\beta h \nu) \right) \right], \tag{16}$$

where $\nu$ represents the phonon frequencies of hydrogen in the matrix and $E_H^{sol}$ corresponds to the energy of an hydrogen atom situated in crystal interstitial sites, calculated as follows:

$$E_H^{sol} = E_{cell} - E_{bulk} - E_{H_2}/2 \tag{17}$$

where $E_{cell}$ stands for the energy of a simulation cell of crystal bulk containing one hydrogen situated at an octahedric site, $E_{bulk}$ represents the energy of the same cell without the hydrogen and $E_{H_2}$ is merely the potential energy of one hydrogen molecule. Our simulations gave $E_{H_2} \simeq -4.74$ eV and $E_H^{sol} \simeq 0.17$ eV. Employing the code Phonopy [91], we have estimated that $\nu \simeq 2 \times 10^{13}$ Hz for the three modes in the case of Ni (Appendix Appendix D). The chemical potential can be expressed as :

$$\mu_{sol} = G_{sol} + k_B T \ln \left( X_{int} \right). \tag{18}$$

To validate our model, we computed the hydrogen solubility in Ni at standard pressure, $P_0 = 1$ bar, *i.e.* considering the equilibrium between gazeous hydrogen ($H_g$) at standard pressure and the hydrogen in solution ($H_{sol}$), using Eq. 10. We compare the results obtain to experiments in high purity Ni [83, 86, 52, 51, 85, 82] (see Fig. 10 (a). We obtain a good agreement with the experimental results found in literature [83, 86, 52, 51, 85, 82], although our approach keeps fundamentally basic.

We now examine the effect of nanovoids on the hydrogen solubility. A local solubility near the surface of bubbles can be computed by considering the thermodynamic equilibrium between the gazeous hydrogen inside the cluster ($H_g$, Fig. 10(b)) and the hydrogen solution ($H_{sol}$, Fig. 10(b)). We

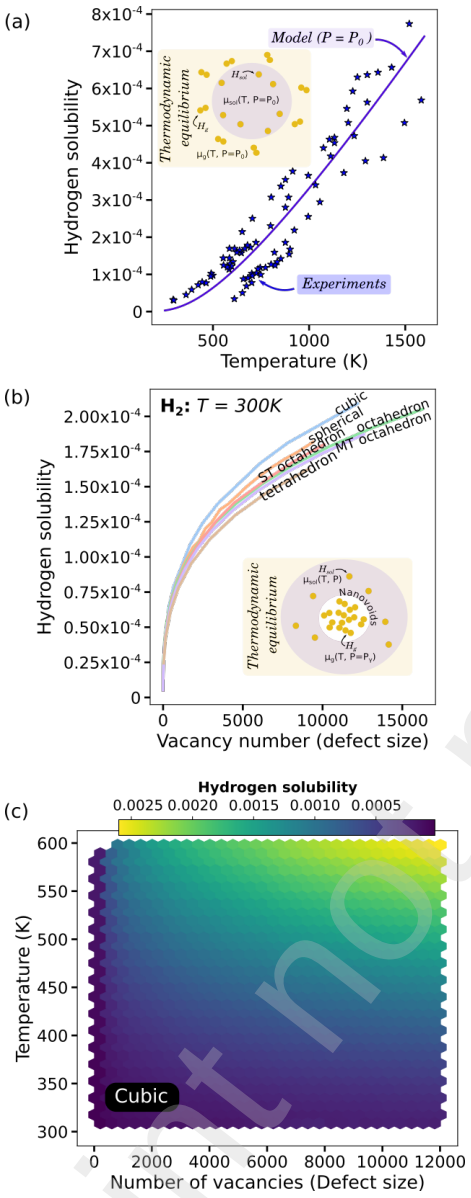


Figure 10: (a) Hydrogen solubility in Ni at standard pressure $P_0$=1 bar modeled by Eq. 10, compared to experiments of high purity Ni [83, 86, 52, 51, 85, 82]. Local hydrogen solubility in Ni near the surface of vacancy cluster, calculated using Eq. 10 (b) for various shapes at a temperature of 300 K against the cluster size expressed in vacancy number, and (c) for cuboid defects against defect size and temperature.

consider that the pressure of such a gas, quoted $P$, is equal to the surface pressure of the nanodefects, $P_\gamma$, (see Appendix Appendix C for justification).

In Fig. 10 (b) we have reported our results for a temperature of 300 K for different shapes of cluster against the number of vacancy involved into the cluster. The local hydrogen solubility, as defined previously, is larger for cuboids in comparison to other cluster shapes. The difference of solubility increases with the number of vacancy involved into the cluster. These results, aligning with conclusions derived from surface energy analysis indicating a cuboid predicted stable shape, provide further argument for the validity of our model. In Fig. 10 (c) we reported the local hydrogen solubility for cuboids against temperature and the number of vacancy involved into the cluster. As expected the solubility increases with temperature.

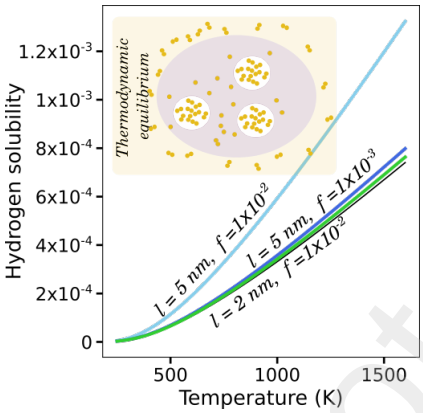


Figure 11: Hydrogen solubility in Ni sample containing a volumic fraction $f$ of cubic shape nanovoid of lenght $l$, model using Eq.19 compared to the solubily of Ni without nanovoids (thin black line, Eq. 10).

Computing the solubility accounting for concentration of clusters of various sizes and shapes is a challenge that would require meso-scale simulations as cluster dynamics or diffusivity models [42, 36]. It will be the purpose of a future study. Nonetheless, as a very first tentative we can merely assumed that the total hydrogen solubility is given by :

$$X_{int} = \gamma \exp\left[-\beta(G_{sol} - \mu_g^0/2\right] + \sum_{s,n_v} f(s,n_v)\gamma \exp\left[-\beta(G_{sol} - \mu_g(P_\gamma(s,n_v))/2)\right] \quad (19)$$

where the total hydrogen contribution comprises two components: one yielded

from the external pressure set at the standard pressure $P_0$, and another yielded from the gaseous hydrogen within nanovoids of shape $s$ and containing $n_v$ vacancies, pressurized at $P_\gamma(s, n_v)$, where $f(s, n_v)$ represents the volumetric fraction of nanovoids. We have simply summed the contributions from the bulk and from the cavities to capture hydrogen. The influence of cubic-shaped nanovoids with lengths $l$ of 2 or 5 nm on solubility is depicted in Fig. 11. Nanovoids below a certain size exhibit negligible influence on hydrogen solubility, even at very high concentrations (as shown by the green line in Fig. 11, where $l = 2$ nm and $f = 1 \times 10^{-2}$). For a size of 5 nm the effect is more pronounced (blue line in Fig. 11, where $l = 5$ nm) even if it requires a high concentration of nanovoids. We expect that nanovoid of 10 nm size (observable in experiments) to have a impact even at lower concentration.

## 5. Conclusion

In summary, our simulations have provided insights into the interplay between hydrogen and nanovoids as well as stacking fault tetrahedra (SFT) in fcc materials. We have observed notable reductions in both formation and surface energies of nanovoids in the presence of hydrogen, in agreement with experiments that observe a stabilization of vacancy clusters by hydrogen [11, 18, 26, 27, 9]. Additionally, the influence of hydrogen on surface energies affect the morphology of nanovoids. The {100} surface emerges as more favorable for hydrogen, such that cubic shapes with {100} surfaces should be predominant according to our predictions. In contrast, the impact of hydrogen on SFT is very less pronounced. We have also noted a screening effect of the long range elastic field of nanovoids in presence of hydrogen, impacting its interaction with other defects which certainly have some implication in material mechanical properties. Our theoretical approach reproduced well the experimental results of high purity Ni [83, 86, 52, 51, 85, 82]. Finally, we determine that the local solubility of hydrogen is maximum around cuboid void and increases with cluster size and with temperature. Although the impact of nanovoids smaller than 5 nm on hydrogen solubility is limited, we anticipate greater efficiency for larger sizes. It would be valuable to apply these findings in a mesoscale framework, such as cluster dynamics, to assess the temporal evolution of cluster populations concerning their size and type relative to hydrogen concentration and temperature [42, 36]. These results contribute to our understanding of hydrogen-material interactions, offering a

foundation for future materials engineering efforts in hydrogen-rich environments.

**Acknowledgements**

We are extremely grateful to Dr. Laurent Proville, whose feedback and active review of the paper have greatly improved its readability. The computational resources utilized for this study were graciously provided by the MCIA (MĂŠsocentre de Calcul Intensif Aquitain) and the Noether computing facilities at La Rochelle University, hosted at the LaSIE laboratory. Additionally, we extend our gratitude to GENCI - (CINES/CCRT) computer center, under Grant number A0110913037.

## Appendix A. Formation energy of vacancy clusters

The formation energy of the n-vacancy defect computed using Eq. 2. Results for Ag and Pd are shown Fig. A.12 and those for Al and Cu Fig. A.13. The formation energy increases with the defect size, and the rate of this increase varies with the nanovoid shape.

DFT investigations in pure metals have revealed that elevated concentrations of hydrogen intensify its entrapment by vacancies [89]. This encourages the creation of superabundant vacancies, where all six octahedral sites adjacent to the vacancy are filled with hydrogen. To assess the influence of hydrogen pressure, we examined a scenario where each vacancy was substituted with six hydrogen atoms. In practice, these additional hydrogen atoms were positioned at the first octahedral sites neighboring the metal atoms that were extracted. Fig. A.14 shows the formation energy for various H - vacancy cluster shapes and the size (number of vacancies) in Ni systems.

## Appendix B. Surface energy of defects

The surface energy of defects, for the other metals studie, quoted $\Gamma_d$ and defined as follows:

$$\Gamma_d = \frac{e_f^n}{S_d}, \tag{B.1}$$

where $S_d$ represents the surface area of the defects. This area is determined from the atomic configurations of the relaxed defect cells using the alpha-shape algorithm, which is implemented in OVITO [87]. Surface energies of Cu & Au are plotted Fig. B.15 and those for Ag & Pd Fig. B.16.

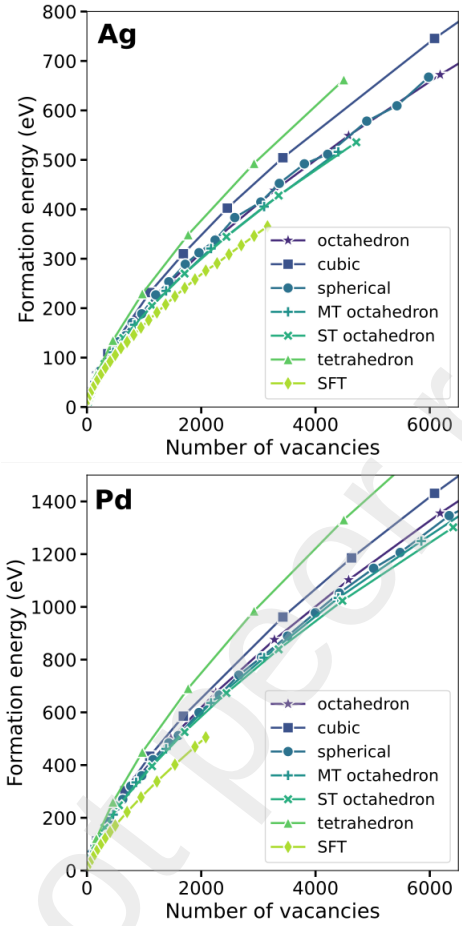


Figure A.12: Formation energy for various vacancy cluster shapes, *i.e* octahedron, cubic, spherical, moderately truncated (MT) octahedron, severely truncated (ST) octahedron, tetrahedron and stacking fault tetrahedra (SFT), and the size (number of vacancies) in Ag and Pd.

Since the surface energy strongly depends on the presence of hydrogen [5, 25, 43, 92] we computed the primary surface energies $\gamma_{110}$, and $\gamma_{111}$ for different hydrogen absorption sites, conventionally referred to as Top, 4F, PT, SB, LB, etc. for {110} planes (Fig. 8(b)) and HCP, FCC, Top sites for {111} planes [5, 25, 43, 92] (Fig. B.20).One can note that Bridge sites are note found to be stable in {111} planes with this potential. Additionally, we considered the impact of the ratio of the number of hydrogen atoms, denoted as $N_H$, to the number of surface Ni atoms, denoted as $N_{Ni}$. To achieve

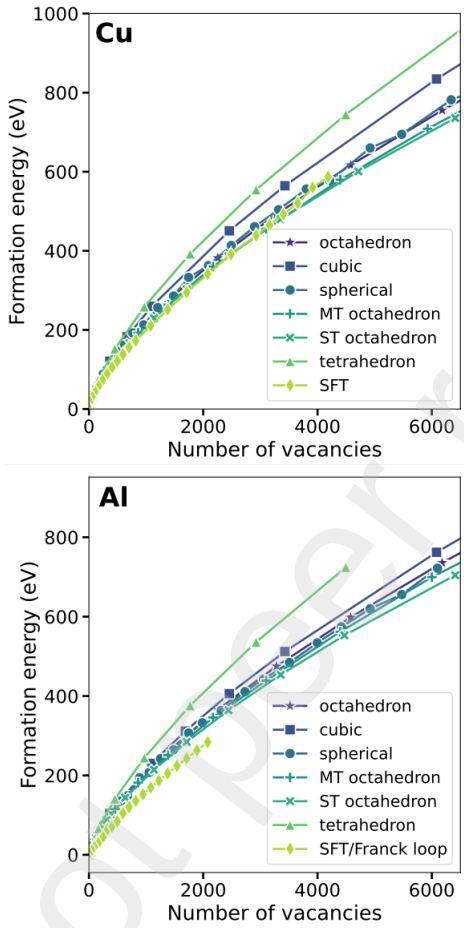


Figure A.13: Formation energy for various vacancy cluster shapes, *i.e* octahedron, cubic, spherical, moderately truncated (MT) octahedron, severely truncated (ST) octahedron, tetrahedron and stacking fault tetrahedra (SFT), and the size (number of vacancies) in Cu and Al.

this, we constructed simulations with free surfaces containing symmetrically distributed hydrogen atoms.

## Appendix C. Determination of the hydrogen gaz pressure

The total free energy of the system, $G_{tot}$, is :

$$G_{tot} = Q + G_g + G_{sol} + \int \gamma_d dA \tag{C.1}$$

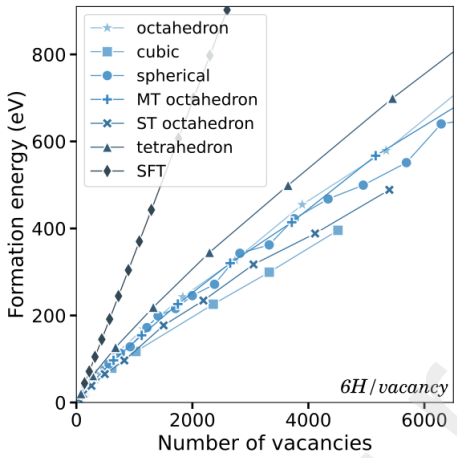


Figure A.14: Formation energy for various H - vacancy cluster shapes and the size (number of vacancies) in Ni systems. Results for another hydrogen concentration is shown Fig. 3(c).

where

$$Q = \frac{1}{2}\int_{V}^{+\infty} \sigma_{ij}\epsilon_{ij} dV \tag{C.2}$$

is the elastic strain energy related to the stress tensor $\sigma_{ij}$ and the strain tensor $\epsilon_{ij}$, $G_g$ is the free energy of hydrogen gaz and $G_{sol}$ is the free energy of the unstrained crystal less the total surface energy of the defects $\int \gamma_d dA$.

Following the work of Nelson *et al.* [63], the equilibrium volume of the defect depends on the elastic strain parameter, quoted $q$, the total number of vacancies in the defect, quoted $n_v$ and the defect shape, $s$. The free energy $G_{sol}$, corresponding to perfect crystal is invariant with $q$, $n_v$ and $s$ such that $\left(\frac{\partial G_{sol}}{\partial q}\right)_{n_v,s} = \left(\frac{\partial G_{sol}}{\partial n_v}\right)_{q,s} = \left(\frac{\partial G_{sol}}{\partial s}\right)_{n_v,q} = 0$.

The minimum total free energy with respect to these parameter, considering that there is a net flow of point defects to or from the clusters, according to the elastic strain field, occurs when the elastic energy passes through a minimum at zero, *i.e.* with $Q = q = 0$ [63], hence when :

$$\begin{cases} \left(\frac{\partial G_g}{\partial q}\right)_{n_v,s} + \left(\frac{\partial \int \gamma_d dA}{\partial q}\right)_{n_v,s} = 0 \\ \left(\frac{\partial G_g}{\partial n_v}\right)_{s,q=0} + \left(\frac{\partial \int \gamma_d dA}{\partial n_v}\right)_{s,q=0} = 0 \\ \left(\frac{\partial \int \gamma_d dA}{\partial s}\right)_{n_v,q=0} = 0 \end{cases} \tag{C.3}$$

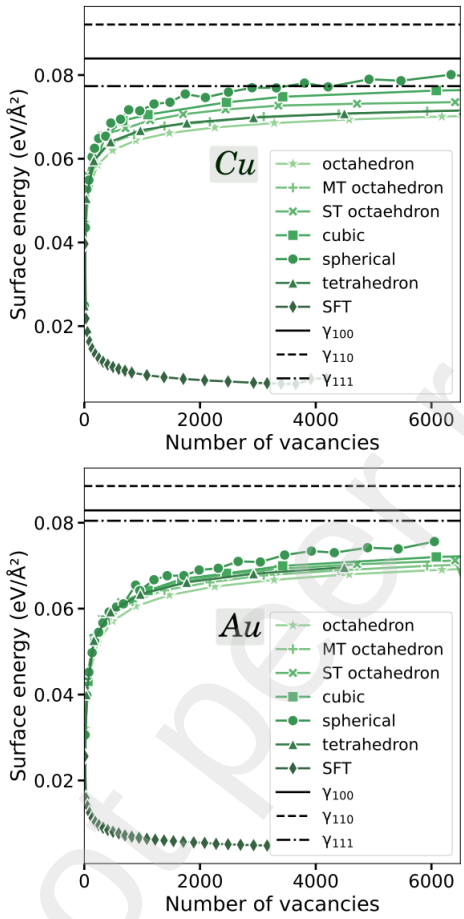


Figure B.15: Surface energy of defects in Cu and Au compared to the surface energy of free surfaces ($\gamma_{100}, \gamma_{110}, \gamma_{111}$).

One notes that $\left(\frac{\partial \int \gamma_d dA}{\partial s}\right)_{n_v, q=0} = 0$ merely means that the shapes of the

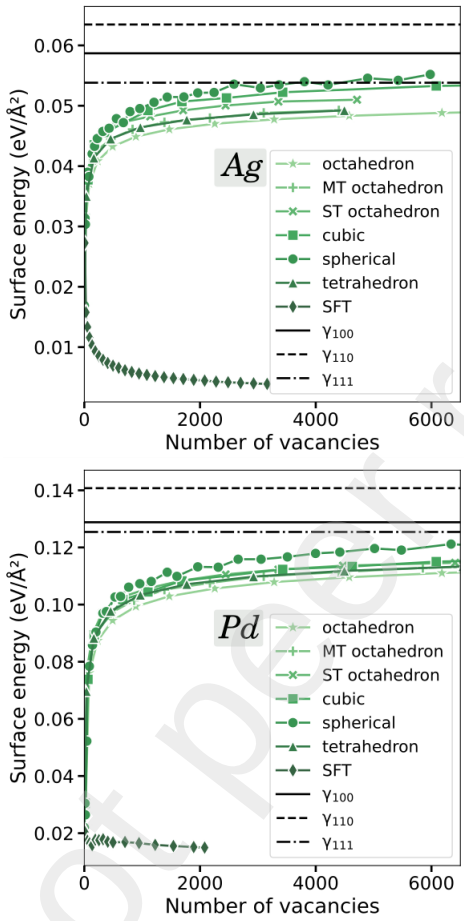


Figure B.16: Surface energy of defects in Ag and Pd compared to the surface energy of free surfaces ($\gamma_{100}, \gamma_{110}, \gamma_{111}$).

defects corresponds to the one that minimize its surface energy. So finally :

$$\begin{aligned} &\left(\frac{\partial G_g}{\partial q}\right)_{n_v,s}\left(\frac{\partial q}{\partial V}\right)_{n_v,s} + \\ &\left(\frac{\partial \int \gamma_d dA}{\partial q}\right)_{n_v,s}\left(\frac{\partial q}{\partial V}\right)_{n_v,s} + \\ &\left(\frac{\partial G_g}{\partial n_v}\right)_{s,q=0}\left(\frac{\partial n_v}{\partial V}\right)_{s,q=0} + \\ &\left(\frac{\partial \int \gamma_d dA}{\partial n_v}\right)_{s,q=0}\left(\frac{\partial n_v}{\partial V}\right)_{s,q=0} = 0 \end{aligned} \tag{C.4}$$

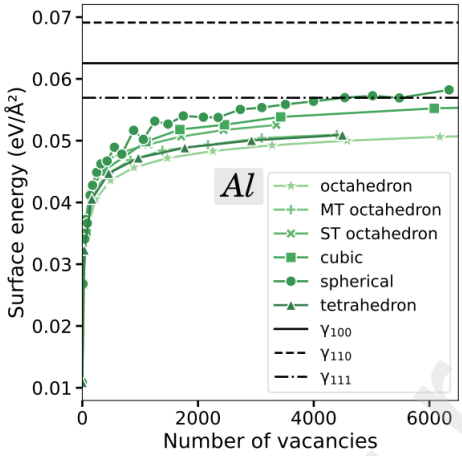


Figure B.17: Surface energy of defects in Al [47] compared to the surface energy of free surfaces $(\gamma_{100}, \gamma_{110}, \gamma_{111})$.

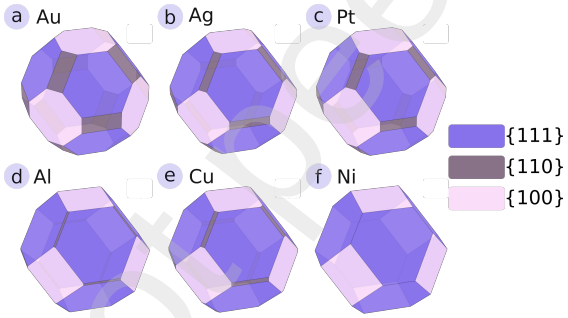


Figure B.18: Wulff construction computed with the surface energy of Table 1 [76] for (a) Au, (b) Ag, (c) Pt, (d) Al, (e) Cu and (f) Ni.

This can be written in term of volume derivative :

$$\left(\frac{\partial G_g}{\partial V}\right)_s + \left(\frac{\partial}{\partial V}\int \gamma_d dA\right)_s = 0 \tag{C.5}$$

where $P_\gamma = \left(\frac{\partial}{\partial V}\int \gamma_d dA\right)_{T,s}$ corresponds to the 'surface-energy pressure' which come from the volume stresses created by relaxation of atoms near the surface of the nanovoid and $P = -\left(\frac{\partial G_g}{\partial V}\right)_T$ is the pressure of the hydrogen gaz at a temperature $T$.

Finally, we have:

$$P = P_\gamma \tag{C.6}$$

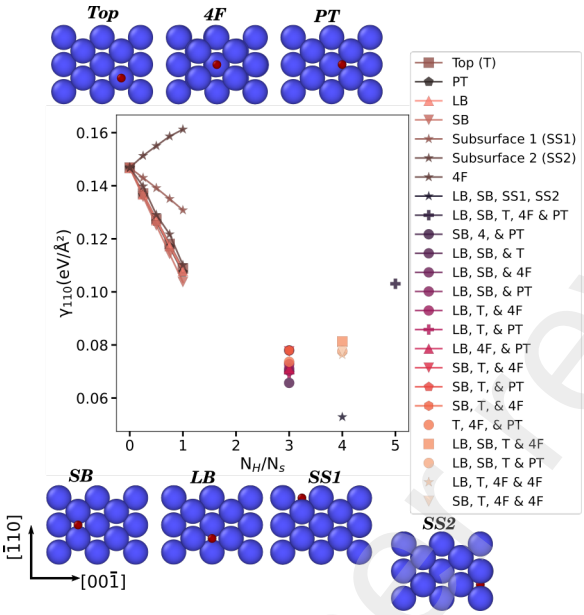


Figure B.19: Surface energy for {110} surface computed for Ni according to the site occupied by the hydrogen atom on the surface (Top (T), 4F, PT, SB, LB, subsurface (SS1 or SS2)) or a combination of these sites and the ratio of the number of hydrogen atoms, quoted $N_H$ (atom colored in red on the atomic configuration of the surface on the top of the figure), to the number of surface Ni atoms, $N_{Ni}$ (atoms colored in blue on the atomic configuration of the surface on the top of the figure).

One notes that $P_\gamma$ can be directly extracted from our atomistic simulations using the Viriel method implemented in LAMMPS [72]. Results of $P_\gamma$ according the number of vacancies, $n_v$, is shown Fig. C.21(a). The surface pressure increases with the defect size, so with $n_v$.

It is worth noticing that there is a linear relationship between $P_\gamma$ and the $n_v^n$, that is not exactly the one commonly used for calculating the surface energy and pressure of nanovoids in the frame of the capillary approximation $2\gamma/R$, with $R$ the radius. The relation that we found is that :

$$P_\gamma \simeq cst \times \frac{\gamma_d}{a_0 n_v^n} \tag{C.7}$$

the value of $n = 0.6$ and the constant depends on the metals (Au $\rightarrow 3 \times 10^{-5} a_0(\text{Å})$; Ag, Al, Cu and Ni $\rightarrow 1 \times 10^{-5} a_0(\text{Å})$; Pd $\rightarrow 2.3 \times 10^{-5} a_0(\text{Å})$).

Fig. C.21(b) shows that linear tendency obtained.

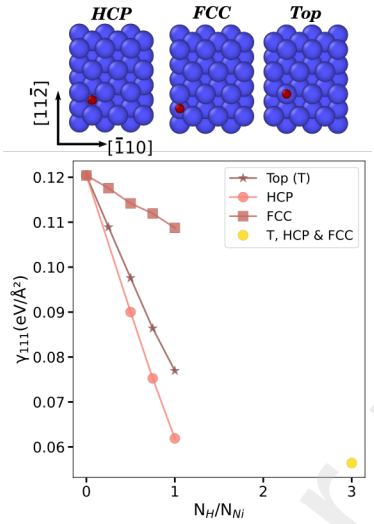


Figure B.20: Surface energy for {111} surface computed for Ni according to the site occupied by the hydrogen atom on the surface (HCP, FCC, Top (T)) or a combination of these sites and the ratio of the number of hydrogen atoms, quoted $N_H$ (atom colored in red on the atomic configuration of the surface on the top of the figure), to the number of surface Ni atoms, $N_{Ni}$ (atoms colored in blue on the atomic configuration of the surface on the top of the figure) One can note that the Bridge position is unstable with this potential.

## Appendix D. Phonon calculations

The phonopy package [91] enables us to compute the density of states for the $H_2$ molecule and Ni crystal with a single hydrogen solute occupying an interstitial octahedral site (Fig. D.22 (a)). Additionally, we determine the dispersion relation for the Ni crystal with a hydrogen solute in octahedral site along high-symmetry points (Fig. D.22 (b)). The phonon frequency of the $H_2$ molecule is found to be $\nu_{H_2} = 13.18 \times 10^{13}$ Hz and $\nu \simeq 2 \times 10^{13}$ Hz, for the phonon frequencies of hydrogen in the matrix for the three modes. These results align well with DFT simulations [109, 53, 92].

## References

[1] D.S. Aidhy, C. Lu, K. Jin, H. Bei, Y. Zhang, L. Wang, and W.J. Weber. Formation and growth of stacking fault tetrahedra in Ni via vacancy aggregation mechanism. *Scripta Mater.*, 114:137–141, 2016. doi: 10.1016/j.scriptamat.2015.12.020.

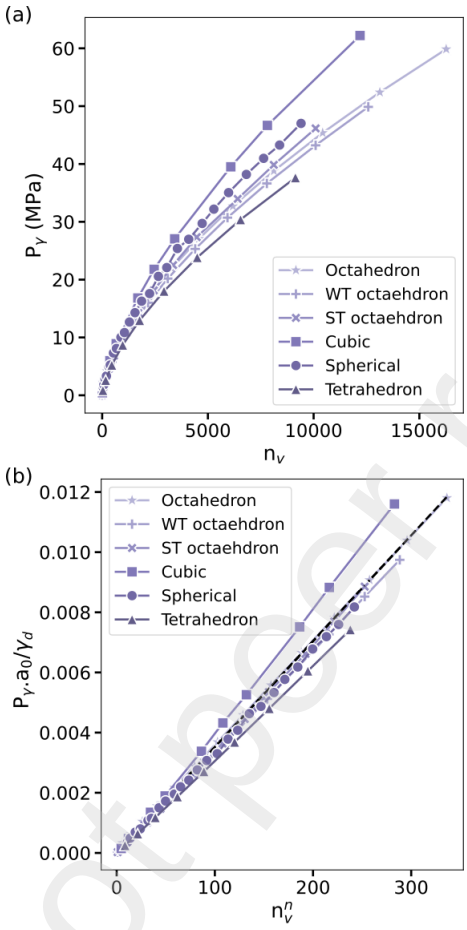


Figure C.21: (a) Surface energy pressure, $P_\gamma$ of Ni for several defect shapes. (b) Variation of $P_\gamma.a_0/\gamma_d$ as a function of the number of vacancies $n_v$ exponent $n = 0.6$ in case of Ni.

[2] J.E. Angelo, N.R. Moody, and M.I. Baskes. Trapping of hydrogen to lattice defects in nickel. *Modelling Simul. Mater. Sci. Eng.*, 3(3):289, 1995. doi: 10.1088/0965-0393/3/3/001.

[3] D.J. Bacon and Y.N. Osetsky. The atomic-scale modeling of dislocation-obstacle interactions in irradiated metals. *JOM*, 59(4):40–45, 2007. doi: 10.1007/s11837-007-0053-0.

[4] Z.J. Bergstrom, D. Perez, and O. El-Atwani. Helium bubble facetation in tungsten thin films. *Scr. Mater.*, 220:114918, 2022. doi: 10.1016/j.scriptamat.2022.114918.

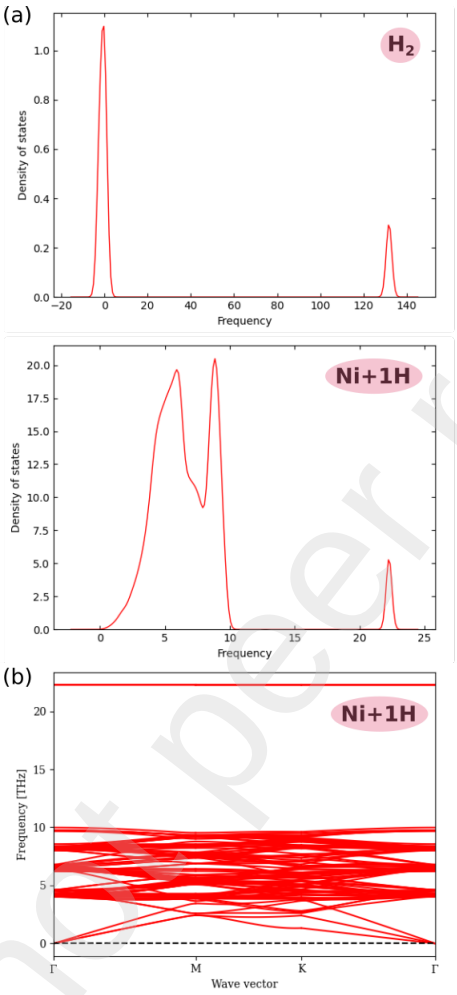


Figure D.22: (a) Phonon density of states of $H_2$ molecule and Ni crystal with one hydrogen solute in interstitial octahedral site. (b) Phonon dispersion relation of Ni crystal with one hydrogen solute in interstitial octahedral site along high symetry points.

[5] B. Bhatia and D.S. Sholl. Chemisorption and diffusion of hydrogen on surface and subsurface sites of flat and stepped nickel surfaces. *J. Chem. Phys.*, 122(20), 2005. doi: https://doi.org/10.1063/1.1902943.

[6] E. Bitzek, P. Koskinen, F. Gähler, M. Moseler, and P. Gumbsch. Structural relaxation made simple. *Phys. Rev. letters*, 97(17):170201, 2006. doi: 10.1103/PhysRevLett.97.170201.

[7] L. Bourgeois, Y. Zhang, Z. Zhang, Y. Chen, and N.V. Medhekar. Transforming solid-state precipitates via excess vacancies. *Nat. Comm.*, 11 (1):1–10, 2020. doi: 10.1038/s41467-020-15087-1.

[8] R.H. Bricknell and D.A. Woodford. The mechanism of cavity formation during high temperature oxidation of nickel. *Acta Metall.*, 30(1):257–264, 1982. ISSN 0001-6160. doi: 10.1016/0001-6160(82)90064-5.

[9] A. Chaudhuri, M.A. Singh, B.J. Diak, C. Cuoppolo, and A.R. Woll. Nanovoid characterization of nominally pure aluminium using synchrotron small angle X-ray scattering (SAXS) methods. *Philos. Mag.*, 93(35):4392–4411, 2013. doi: 10.1080/14786435.2013.832838.

[10] C.W. Chen. The shapes of irradiation-produced voids in nickel. *Phys. Status Solidi A*, 16(1):197–210, 1973. doi: 10.1002/pssa.2210160121.

[11] L.M. Clarebrough, P. Humble, and M.H. Loretto. Voids in quenched copper, silver and gold. *Acta Metall.*, 15(6):1007–1023, 1967. doi: 10.1016/0001-6160(67)90265-9.

[12] C. Dai, Q. Wang, P. Saidi, B. Langelier, C.D. Judge, M.R. Daymond, and M.A. Mattucci. Atomistic structure and thermal stability of dislocation loops, stacking fault tetrahedra, and voids in face-centered cubic fe. *J. Nucl. Mater.*, 563:153636, 2022. doi: 10.1016/j.jnucmat.2022.153636.

[13] Y. Dai and M. Victoria. Defect structures in deformed FCC metals. *Acta Mater.*, 45(8):3495–3501, 1997. doi: 10.1016/S1359-6454(97)00019-0.

[14] D. Di Stefano, M. Mrovec, and C. Elsässer. First-principles investigation of quantum mechanical effects on the diffusion of hydrogen in iron and nickel. *Phys. Rev. B*, 92(22):224301, 2015. doi: 10.1103/PhysRevB.92.224301.

[15] F.J. Dominguez-Gutierrez, P. Grigorev, A. Naghdi, J. Byggmastar, G.Y. Wei, T.D. Swinburne, S. Papanikolaou, and M.J. Alava. Nanoindentation of tungsten: From interatomic potentials to dislocation plasticity mechanisms. *Phys. Rev. Mater.*, 7(4):043603, 2023. doi: doi.org/10.1103/PhysRevMaterials.7.043603.

[16] J. DĂŠrĂ¨s, L. Proville, and M.C. Marinica. Dislocation depinning from nano-sized irradiation defects in a bcc iron model. *Acta Mater.*, 99:99–105, 2015. doi: 10.1016/j.actamat.2015.07.067.

[17] H.E. Evans. Cavity formation and metallurgical changes induced by growth of oxide scale. *Mater. Sci. Technol.*, 4(12):1089–1098, 1988. doi: 10.1179/mst.1988.4.12.1089.

[18] B.L. Eyre. Transmission electron microscope studies of point defect clusters in fcc and bcc metals. *J. Phys. F: Met. Phys.*, 3(2):422, 1973. doi: 10.1088/0305-4608/3/2/009.

[19] X. Feaugas and D. Delafosse. Hydrogen and crystal defects interactions: Effects on plasticity and fracture. In *Mechanics-Microstructure-Corrosion Coupling*, pages 199–222. Elsevier, 2019. doi: 10.1016/B978-1-78548-309-7.50009-0.

[20] N. Fernandez, Y. Ferro, and D. Kato. Hydrogen diffusion and vacancies formation in tungsten: density functional theory calculations and statistical models. *Acta Mater.*, 94:307–318, 2015. doi: 10.1016/j.actamat.2015.04.052.

[21] M. Fokt, G. Adjanor, and T. Jourdan. A variable-gap model for helium bubbles in nickel. *Comput. Mater. Sci.*, 202:110921, 2022. doi: 10.1016/j.commatsci.2021.110921.

[22] V. Fotopoulos, R. Grau-Crespo, and AL Shluger. Thermodynamic analysis of the interaction between metal vacancies and hydrogen in bulk cu. *Phys. Chem. Chem. Phys.*, 25(13):9168–9175, 2023. doi: 10.1039/D3CP00085K.

[23] Y. Fukai. Formation of superabundant vacancies in M–H alloys and some of its consequences: a review. *J. Alloys Compd.*, 356:263–269, 2003. doi: 10.1016/S0925-8388(02)01269-0.

[24] M.G. Ganchenkova, Y.N. Yagodzinskyy, V.A. Borodin, and H. Hänninen. Effects of hydrogen and impurities on void nucleation in copper: simulation point of view. *Philos. Mag.*, 94(31):3522–3548, 2014. doi: 10.1080/14786435.2014.962642.

[25] J. Greeley and M. Mavrikakis. A first-principles study of surface and subsurface h on and in ni (1 1 1): diffusional properties and coverage-dependent behavior. *Surf. Sci.*, 540(2-3):215–229, 2003. doi: https://doi.org/10.1016/S0039-6028(03)00790-8.

[26] G. Hachet, A. Metsue, A. Oudriss, and X. Feaugas. Influence of hydrogen on the elastic properties of nickel single crystal: A numerical and experimental investigation. *Acta Mater.*, 148:280–288, 2018. doi: 10.1016/j.actamat.2018.01.056.

[27] G. Hachet, A. Oudriss, A. Barnoush, T. Hajilou, D. Wang, A. Metsue, and X. Feaugas. Antagonist softening and hardening effects of hydrogen investigated using nanoindentation on cyclically pre-strained nickel single crystal. *Mater. Sci. Eng. A*, 803:140480, 2021. doi: 10.1016/j.msea.2020.140480.

[28] L.M. Hale, B.M. Wong, J.A. Zimmerman, and X.W. Zhou. Atomistic potentials for palladium–silver hydrides. *Modelling Simul. Mater. Sci. Eng.*, 21(4):045005, 2013. doi: 10.1088/0965-0393/21/4/045005.

[29] T. Hatano and H. Matsui. Molecular dynamics investigation of dislocation pinning by a nanovoid in copper. *Phys. Rev. B*, 72(9):094105, 2005. doi: 10.1103/PhysRevB.72.094105.

[30] K.R. Hebert, J.H. Ai, G.R. Stafford, K.M. Ho, and C.Z. Wang. Vacancy defects in aluminum formed during aqueous dissolution. *Electrochim. Acta*, 56(4):1806–1809, 2011. doi: 10.1016/j.electacta.2010.08.052.

[31] E.A. Hodille, N. Fernandez, Z.A. Piazza, M. Ajmalghan, and Y. Ferro. Hydrogen supersaturated layers in h/d plasma-loaded tungsten: A global model based on thermodynamics, kinetics and density functional theory data. *Phys. Rev. Mater.*, 2(9):093802, 2018. doi: 10.1103/PhysRevMaterials.2.093802.

[32] A. Howie and L.D. Marks. Elastic strains and the energy balance for multiply twinned particles. *Philos. Mag. A*, 49(1):95–109, 1984. doi: 10.1080/01418618408233432.

[33] R.A. Johnson. Calculations of small vacancy and interstitial clusters for an fcc lattice. *Phys. Rev. B*, 152(2):629, 1966. doi: 10.1103/PhysRev.152.629.

[34] R.A. Johnson. Calculations for the stability of voids, stacking-fault tetrahedra, and dislocation loops in nickel. *Philos. Mag.*, 16(141):553–564, 1967. doi: 10.1080/14786436708220864.

[35] T. Jossang and J.P. Hirth. The energies of stacking-fault teirahedra in fcc metals. *Philos. Mag.*, 13(124):657–670, 1966. doi: 10.1080/14786436608212687.

[36] T. Jourdan, G. Bencteux, and G. Adjanor. Efficient simulation of kinetics of radiation induced defects: A cluster dynamics approach. *J. Nucl. Mater.*, 444(1-3):298–313, 2014. doi: 10.1016/j.jnucmat.2013.10.009.

[37] T. Kadoyoshi, H. Kaburaki, F. Shimizu, H. Kimizuka, S. Jitsukawa, and J. Li. Molecular dynamics study on the formation of stacking fault tetrahedra and unfaulting of frank loops in fcc metals. *Acta Mater.*, 55 (9):3073–3080, 2007. doi: 10.1016/j.actamat.2007.01.010.

[38] M. Kiritani. Story of stacking fault tetrahedra. *Mater. Chem. Phys.*, 50(2):133–138, 1997. doi: 10.1016/S0254-0584(97)80250-7.

[39] M. Kiritani. Similarity and difference between fcc, bcc and hcp metals from the view point of point defect cluster formation. *J. Nucl. Mater.*, 276(1-3):41–49, 2000. doi: 10.1016/S0022-3115(99)00167-1.

[40] M. Kiritani, Y. Shimomura, and S. Yoshida. Shape of voids in quenched aluminum. *J. Phys. Soc. Jpn.*, 19(9):1624–1631, 1964. doi: 10.1143/JPSJ.19.1624.

[41] M. Kiritani, T. Sota, T. Tawara, H. Arimura, K. Yasunaga, Y. Matsukawa, and M. Komatsu. Defect structures introduced in fcc metals by high-speed deformation. *Radiat. Eff. Defects Solids*, 157(1-2):53–74, 2002. doi: 10.1080/10420150211397.

[42] A.A. Kohnert and B.D. Wirth. Cluster dynamics models of irradiation damage accumulation in ferritic iron. i. trap mediated interstitial cluster diffusion. *J. Appl. Phys.*, 117(15), 2015. doi: 10.1063/1.4918315.

[43] G. Kresse and J. Hafner. First-principles study of the adsorption of atomic h on ni (111),(100) and (110). *Surf. Sci.*, 459(3):287–302, 2000. doi: 10.1016/S0039-6028(00)00457-X.

[44] M. Landeiro Dos Reis, L. Proville, and M. Sauzay. Modeling the climb-assisted glide of edge dislocations through a random distribution of nanosized vacancy clusters. *Phys. Rev. Mater.*, 2(9):093604, 2018. doi: 10.1103/PhysRevMaterials.2.093604.

[45] M. Landeiro Dos Reis, L. Proville, M.C. Marinica, and M. Sauzay. Atomic scale simulations for the diffusion-assisted crossing of dislocation anchored by vacancy clusters. *Phys. Rev. Mater.*, 4(10):103603, 2020. doi: 10.1103/PhysRevMaterials.4.103603.

[46] Emanuel A Lazar, Jiayin Lu, and Chris H Rycroft. Voronoi cell analysis: The shapes of particle systems. *American Journal of Physics*, 90 (6):469–480, 2022. doi: 10.1119/5.0087591.

[47] X.Y. Liu, F. Ercolessi, and J.B. Adams. Aluminium interatomic potential from density functional theory calculations with improved stacking fault energy. *Modelling Simul. Mater. Sci. Eng.*, 12(4):665, 2004. doi: 10.1088/0965-0393/12/4/007.

[48] M.H. Loretto, P.J. Phillips, and M.J. Mills. Stacking fault tetrahedra in metals. *Scr. Mater.*, 94:1–4, 2015. doi: 10.1016/j.scriptamat.2014.07.020.

[49] G. Lu and E. Kaxiras. Hydrogen embrittlement of aluminum: the crucial role of vacancies. *Physical review letters*, 94(15):155501, 2005. doi: 10.1103/PhysRevLett.94.155501.

[50] L.D. Marks. Modified wulff constructions for twinned particles. *J. Cryst. Growth*, 61(3):556–566, 1983. doi: 10.1016/0022-0248(83)90184-7.

[51] R.B McLellan and W.A Oates. The solubility of hydrogen in rhodium, ruthenium, iridium and nickel. *Acta Metall.*, 21(3):181–185, 1973. ISSN 0001-6160. doi: https://doi.org/10.1016/0001-6160(73)90001-1.

[52] R.B McLellan and P.L. Sutter. Thermodynamics of the hydrogen-nickel system. *Acta Metall.*, 32(12):2233–2239, 1984. ISSN 0001-6160. doi: https://doi.org/10.1016/0001-6160(84)90165-2.

[53] A. Metsue, A. Oudriss, J. Bouhattate, and X. Feaugas. Contribution of the entropy on the thermodynamic equilibrium of vacancies in nickel. *J Chem. Phys.*, 140(10), 2014. doi: 10.1063/1.4867543.

[54] A. Metsue, A. Oudriss, and X. Feaugas. Displacement field induced by a vacancy in nickel and some implications for the solubility of hydrogen. *Philos. Mag.*, 94(34):3978–3991, 2014. doi: 10.1080/14786435.2014.975769.

[55] A. Metsue, A. Oudriss, and X. Feaugas. Hydrogen solubility and vacancy concentration in nickel single crystals at thermal equilibrium: New insights from statistical mechanics and ab initio calculations. *J. Alloys Compd*, 656:555–567, 2016. doi: 10.1016/j.jallcom.2015.09.252.

[56] A. Metsue, A. Oudriss, and X. Feaugas. Trapping/detrapping kinetic rates of hydrogen around a vacancy in nickel and some consequences on the hydrogen-vacancy clusters thermodynamic equilibrium. *Comput. Mater. Sci.*, 151:144–152, 2018. doi: 10.1016/j.commatsci.2018.05.013.

[57] M. Militzer, W.P. Sun, and J.J. Jonas. Modelling the effect of deformation-induced vacancies on segregation and precipitation. *Acta Metall. Mater.*, 42(1):133–141, 1994. doi: 10.1016/0956-7151(94)90056-6.

[58] Y. Mishin, M.J. Mehl, D.A. Papaconstantopoulos, A.F. Voter, and J.D. Kress. Structural stability and lattice defects in copper: Ab initio, tight-binding, and embedded-atom calculations. *Phys. Rev. B*, 63(22): 224106, 2001. doi: 10.1103/PhysRevB.63.224106.

[59] B. Molleman and T. Hiemstra. Size and shape dependency of the surface energy of metallic nanoparticles: unifying the atomic and thermodynamic approaches. *Phys. Chem. Chem. Phys.*, 20(31):20575–20587, 2018. doi: 10.1039/C8CP02346H.

[60] I. Mukouda, Y. Shimomura, and M. Kiritani. Cryo-transfer TEM study of vacancy cluster formation in thin films of aluminum and copper elongated at low temperature. *Mater. Sci. Eng. A*, 350(1-2):37–43, 2003. doi: 10.1016/S0921-5093(02)00704-9.

[61] M. Nagumo. *Fundamentals of hydrogen embrittlement*, volume 921. Springer, 2016.

[62] R. Nazarov, T. Hickel, and J. Neugebauer. Ab initio study of H-vacancy interactions in fcc metals: Implications for the formation of superabundant vacancies. *Phys. Rev. B*, 89(14):144108, 2014. doi: 10.1103/PhysRevB.89.144108.

[63] R.S. Nelson, D.J. Mazey, and R.S. Barnes. The thermal equilibrium shape and size of holes in solids. *Philos. Mag.*, 11(109):91–111, 1965. doi: 10.1080/14786436508211927.

[64] J.K. Nørskov, F. Besenbacher, J. Bøttiger, B.B. Nielsen, and A.A. Pisarev. Interaction of hydrogen with defects in metals: Interplay between theory and experiment. *Phys. Rev. Letters*, 49(19):1420, 1982. doi: 10.1103/PhysRevLett.49.1420.

[65] R.P. Oleksak, M. Kapoor, D. Perea, G.R. Holcomb, and Ö.N. Doğan. The role of metal vacancies during high-temperature oxidation of alloys. *NPJ Mater. Degrad.*, 2(1):1–8, 2018. doi: 10.1038/s41529-018-0046-1.

[66] K. Ono and T. Kino. Thermal generation of vacancies from voids in aluminium. *Philos. Mag. A*, 81(11):2565–2575, 2001. doi: 10.1080/01418610108216655.

[67] Y.N. Osetsky, M. Victoria, A. Serra, S.I. Golubov, and V. Priego. Computer simulation of vacancy and interstitial clusters in bcc and fcc metals. *J. Nucl. Mater.*, 251:34–48, 1997. doi: 10.1016/S0022-3115(97)00255-9.

[68] Y.N. Osetsky, D.J. Bacon, A. Serra, B.N. Singh, and S.I. Golubov. Stability and mobility of defect clusters and dislocation loops in metals. *J. Nucl. Mater.*, 276(1-3):65–77, 2000. doi: 10.1016/S0022-3115(99)00170-1.

[69] Y.N. Osetsky, R.E. Stoller, D. Rodney, and D.J. Bacon. Atomic-scale details of dislocation–stacking fault tetrahedra interaction. *Mater. Sci. Eng. A*, 400:370–373, 2005. doi: 10.1016/j.msea.2005.03.038.

[70] A.K. Panda, R. Divakar, A. Singh, R. Thirumurugesan, and P. Parameswaran. Molecular dynamics studies on formation of stacking fault tetrahedra in fcc metals. *Comput. Mater. Sci.*, 186:110017, 2021. doi: 10.1016/j.commatsci.2020.110017.

[71] S. Perusin, B. Viguier, D. Monceau, L. Ressier, and E. Andrieu. Injection of vacancies at metal grain boundaries during the oxidation of nickel. *Acta Mater.*, 52(18):5375–5380, 2004. doi: 10.1016/j.actamat.2004.07.043.

[72] S. Plimpton. Fast parallel algorithms for short-range molecular dynamics. *J. Comput. Phys.*, 117(1):1–19, 1995. doi: 10.1006/jcph.1995.1039.

[73] J. Polák. Production, annihilation and migration of point defects in cyclic straining. *Materialia*, 14:100938, 2020. doi: 10.1016/j.mtla.2020.100938.

[74] J.M. Polfus, O.M. Lovvik, R. Bredesen, and T. Peters. Hydrogen induced vacancy clustering and void formation mechanisms at grain boundaries in palladium. *Acta Mater.*, 195:708–719, 2020. doi: 10.1016/j.actamat.2020.06.007.

[75] G.P.P. Pun. to be published (the potential is on the web Interatomic Potentials Repository").

[76] J Magnus Rahm and Paul Erhart. Wulffpack: A python package for wulff constructions. *Journal of Open Source Software*, 5(45):1944, 2020. doi: 10.21105/joss.01944.

[77] J.S. Robach, I.M. Robertson, H.J. Lee, and B.D. Wirth. Dynamic observations and atomistic simulations of dislocation–defect interactions in rapidly quenched copper and gold. *Acta Mater.*, 54(6):1679–1690, 2006. doi: 10.1016/j.actamat.2005.11.038.

[78] J. L. Rodríguez-López, J. M. Montejano-Carrizales, U. Pal, J. F. Sánchez-Ramírez, H. E. Troiani, D. García, M. Miki-Yoshida, and M. José-Yacamán. Surface reconstruction and decahedral structure of bimetallic nanoparticles. *Phys. Rev. Lett.*, 92: 196102, May 2004. doi: 10.1103/PhysRevLett.92.196102. URL `https://link.aps.org/doi/10.1103/PhysRevLett.92.196102`.

[79] E. Ruedl, P. Delavignette, and S. Amelinckx. Electron microscopic study of dislocations and fission damage in platinum foils. *J. Nucl. Mater.*, 6(1):46–68, 1962. doi: 10.1016/0022-3115(62)90215-5.

[80] R. Schäublin*, Z. Yao, N. Baluc, and M. Victoria. Irradiation-induced stacking fault tetrahedra in fcc metals. *Philos. Mag.*, 85(4-7):769–777, 2005. doi: 10.1080/14786430412331319929.

[81] Y. Shimomura and S. Yoshida. Heterogeneous nucleation of voids in quenched aluminum. *J. Phys. Soc. Jpn.*, 22(1):319–331, 1967. doi: 10.1143/JPSJ.22.319.

[82] A. Sieverts. Zar kenntnis der okklusion und diffusion von gasen durch metalle. *Zeitschrift fĂźr Physikalische Chemie*, 60U(1):129–201, 1907. doi: doi:10.1515/zpch-1907-6009.

[83] A. Sieverts. Zar kenntnis der okklusion und diffusion von gasen durch metalle. *Zeitschrift für physikalische Chemie*, 60(1):129–201, 1907. doi: 10.1515/zpch-1907-6009.

[84] J. Silcox and P.B. Hirsch. Direct observations of defects in quenched gold. *Philos. Mag.*, 4(37):72–89, 1959. doi: 10.1080/14786435908238228.

[85] J. Smittenberg. Absorption and adsorption of hydrogen by nickel. *Recueil des Travaux Chimiques des Pays-Bas*, 53(12):1065–1083, 1934. doi: https://doi.org/10.1002/recl.19340531202.

[86] S.W. Stafford and R.B. McLellan. The solubility of hydrogen in nickel and cobalt. *Acta Metall.*, 22(12):1463–1468, 1974. doi: 10.1016/0001-6160(74)90107-2.

[87] A. Stukowski. Computational analysis methods in atomistic modeling of crystals. *JOM*, 66(3):399–407, 2014. doi: 10.1007/s11837-013-0827-5.

[88] A. Stukowski, V.V. Bulatov, and A. Arsenlis. Automated identification and indexing of dislocations in crystal interfaces. *Model. Simul. Mater. Sci. Eng.*, 20(8):085007, 2012. doi: 10.1088/0965-0393/20/8/085007.

[89] D. Tanguy, Y. Wang, and D. Connétable. Stability of vacancy-hydrogen clusters in nickel from first-principles calculations. *Acta Mater.*, 78: 135–143, 2014. doi: 10.1016/j.actamat.2014.06.021.

[90] G. Thomas and J. Washburn. Precipitation of vacancies in metals. *Rev. Mod. Phys.*, 35(4):992, 1963. doi: 10.1103/RevModPhys.35.992.

[91] A. Togo, L. Chaput, T. Tadano, and I. Tanaka. Implementation strategies in phonopy and phono3py. *J. Phys. Condens. Matter*, 35(35): 353001, 2023. doi: 10.1088/1361-648X/acd831.

[92] C. Traisnel, A. Metsue, A. Oudriss, J. Bouhattate, and X. Feaugas. Hydrogen solubility and diffusivity near surface of nickel single crystals: Some implications of elastic energy. *Comput. Mater. Sci.*, 188:110136, 2021. doi: 10.1016/j.commatsci.2020.110136.

[93] B.P. Uberuaga, R.G. Hoagland, A.F. Voter, and S.M. Valone. Direct transformation of vacancy voids to stacking fault tetrahedra. *Phys. Rev. letters*, 99(13):135501, 2007. doi: 10.1103/PhysRevLett.99.135501.

[94] C. Varvenne, O. Mackain, and E. Clouet. Vacancy clustering in zirconium: An atomic-scale study. *Acta Mater.*, 78:65–77, 2014. doi: 10.1016/j.actamat.2014.06.012.

[95] C. Varvenne, O. Mackain, L. Proville, and E. Clouet. Hydrogen and vacancy clustering in zirconium. *Acta Mater.*, 102:56–69, 2016. doi: 10.1016/j.actamat.2015.09.019.

[96] T.E. Volin and R.W. Balluffi. Annealing kinetics of voids and the self-diffusion coefficient in aluminum. *physica status solidi (b)*, 25(1): 163–173, 1968. doi: 10.1002/pssb.19680250116.

[97] H. Wang, D.S. Xu, R. Yang, and P. Veyssière. The formation of stacking fault tetrahedra in Al and Cu: I. Dipole annihilation and the nucleation stage. *Acta Mater.*, 59(1):1–9, 2011. doi: 10.1016/j.actamat.2010.07.046.

[98] H. Wang, D.S. Xu, R. Yang, and P. Veyssiere. The formation of stacking fault tetrahedra in Al and Cu: II. Sft growth by successive absorption of vacancies generated by dipole annihilation. *Acta Mater.*, 59(1):10–18, 2011. doi: 10.1016/j.actamat.2010.07.044.

[99] H. Wang, D. Rodney, D.S. Xu, R. Yang, and P. Veyssière. Defect kinetics on experimental timescales using atomistic simulations. *Philos. Mag.*, 93(1-3):186–202, 2013. doi: 10.1080/14786435.2012.674224.

[100] M. Wei, P. Zhang, S. Zhou, X. Wang, G. Wang, and J. Zhao. Vacancy clustering behaviors and stable configurations in vanadium metal: First-principles investigations. *Nuclear Materials and Energy*, 33:101296, 2022. doi: 10.1016/j.nme.2022.101296.

[101] Q. Wei, N. Li, K. Sun, and L.M. Wang. The shape of bubbles in he-implanted cu and au. *Scr. Mater.*, 63(4):430–433, 2010. doi: 10.1016/j.scriptamat.2010.04.043.

[102] P.L. Williams, Y. Mishin, and J.C. Hamilton. An embedded-atom potential for the Cu–Ag system. *Modelling Simul. Mater. Sci. Eng.*, 14 (5):817, 2006. doi: 10.1088/0965-0393/14/5/002.

[103] B.D. Wirth, V. Bulatov, and T. Diaz de La Rubia. Atomistic simulation of stacking fault tetrahedra formation in Cu. *J. Nucl. Mater.*, 283:773–777, 2000. doi: 10.1016/S0022-3115(00)00262-2.

[104] X.L. Wu, B. Li, and E. Ma. Vacancy clusters in ultrafine grained Al by severe plastic deformation. *Appl. Phys. Lett.*, 91(14):141908, 2007. doi: 10.1063/1.2794416.

[105] G. Wulff. Zur frage der geschwindigkeit des wachstums und der auflosung der kristall achen. *Z. Kristallogr*, 34:449–530, 1901.

[106] T. Yang, C. Li, S.J. Zinkle, S. Zhao, H. Bei, and Y. Zhang. Irradiation responses and defect behavior of single-phase concentrated solid solution alloys. *J. Mater. Res.*, 33(19):3077–3091, 2018. doi: 10.1557/jmr.2018.285.

[107] S. Yoshida, M. Kiritani, Y. Shimomura, and A. Yoshinaka. Voids in quenched gold. *J. Phys. Soc. Jpn.*, 20(4):628–629, 1965. doi: 10.1143/JPSJ.20.628.

[108] Z. Zhang, T. Liu, A.E. Smith, N.V. Medhekar, P.N.H. Nakashima, and L. Bourgeois. Mechanisms of void shrinkage in aluminium. *J. Appl. Crystallogr.*, 49(5):1459–1470, 2016. doi: 10.1107/S1600576716010657.

[109] H. Zheng, B.K. Rao, S.N. Khanna, and P. Jena. Electronic structure and binding energies of hydrogen-decorated vacancies in ni. *Phys. Rev. B*, 55(7):4174, 1997. doi: 10.1103/PhysRevB.91.094106.

[110] S.J. Zinkle, W.G. Wolfer, G.L. Kulcinski, and L.E. Seitzman. Ii. effect of oxygen and helium on void formation in metals. *Philos. Mag. A*, 55 (1):127–140, 1987. doi: 10.1080/01418618708209804.